

©2019, Elsevier. Licensed under the Creative Commons Attribution-NonCommercial-NoDerivatives 4.0 International <http://creativecommons.org/about/downloads>



# **Physico-chemical properties of newly discovered hydrothermal plumes above the Southern Mid-Atlantic Ridge (13°-33°S)**

**Florian Schmid<sup>1,2</sup>, Maïke Peters<sup>3,4</sup>, Maren Walter<sup>1,3</sup>, Colin Devey<sup>2</sup>, Sven Petersen<sup>2</sup>, Isobel Yeo<sup>5</sup>, Janna Köhler<sup>1,3</sup>, John W. Jamieson<sup>6</sup>, Sharon Walker<sup>7</sup>, Jürgen Sültenfuß<sup>3</sup>**

<sup>1</sup>MARUM, Center for Marine Environmental Sciences at the University of Bremen, Germany.

<sup>2</sup>GEOMAR, Helmholtz-Center for Ocean Research Kiel, Germany.

<sup>3</sup>IUP, Institute of Environmental Physics at the University of Bremen, Germany.

<sup>4</sup>ICBM, Institute for the Chemistry and Biology of the Marine Environment at the Carl von Ossietzky University of Oldenburg, Germany.

<sup>5</sup>NOCS, National Oceanography Center Southampton, UK.

<sup>6</sup>Memorial University of Newfoundland, St. John's, Canada

<sup>7</sup>NOAA/Pacific Marine Environmental Laboratory, Seattle, USA

Corresponding author: Florian Schmid ([fschmid@geomar.de](mailto:fschmid@geomar.de))

**Key Words:** Southern Mid-Atlantic Ridge, mid-ocean ridges, hydrothermal plumes, helium-3, vent fauna biogeography

## **Abstract**

The oceanic crust is initially cooled and deep-sea chemosynthetic ecosystems are largely fed by hydrothermal circulation and venting on the seafloor. Much of this venting takes place at mid-ocean ridges and in order to make realistic models of the crust's thermal budget and to understand chemosynthetic biogeography it is important to have a detailed inventory of vent sites. Until recently, a major gap in this inventory was the Mid-Atlantic Ridge south of 13°S, a key region for vent fauna biogeography as it is the corridor linking the Atlantic to the Indian and Pacific Oceans. In spring 2013 we systematically surveyed the axial region between 13°S and 33°S for hydrothermal signals in the water column, using turbidity, oxidation-reduction-potential (ORP) and noble gases as indicators. Standard conductivity-temperature-depth (CTD) rosette water-sampler deployments were complimented by a novel autonomous underwater vehicle (AUV) deployment strategy, in which the AUV made single-pass, segment-scale (up to 100 km long) dives close to the seafloor to detect small vents. The ca. 2100 km-long survey covered 16 ridge segments and we identified previously unknown hydrothermal plumes above ten segments that point to 14 new hydrothermal vent fields. The majority of plumes are located at high-relief segment centers, where magmatism is robust. A wide gap in the distribution of vents in the 19°S-23°S region coincides with the Rio de Janeiro Transform, the maximum southward progression of North Atlantic Deep Waters and the maximum northwards extent of <sup>3</sup>He-enriched waters with Pacific origins. Crossflowing currents in the transform and the large gap between adjacent vents may prevent a meridional connection between the vent fauna communities in the North Atlantic and along the Antarctic Ridges. This makes the region a prime target for future biogeographical studies.

## 1 Introduction

Hydrothermal venting along the globe-spanning network of mid-ocean ridges (MORs) is a key process for the transfer of chemical elements and heat from the lithosphere into the ocean. Knowing the location of individual vent fields, their frequency and spacing along the ridge axes, their discharge rates and fluid compositions is crucial to constrain geochemical cycles and the heat budget of the ocean crust (Edmond et al., 1979; Elderfield and Schultz, 1996; Hasterok, 2013; Saito et al., 2013). Hydrothermal vent sites represent oases in the deep sea, as the discharged dissolved and particulate chemicals fuel microbial chemosynthesis that nourishes endemic vent communities (Fisher et al., 2007; Van Dover et al., 2002). Determining the location of individual vent sites is a prerequisite to investigate the regional vent communities and to understand their geographic dispersal and genetic connectivity across different ocean basins (Kelley and Shank, 2010; Shank et al., 1998; Van Dover et al., 2002). Currently, there is a large geographical gap between known vents sites in the equatorial Atlantic and those along the Antarctic and Indian Ocean ridges, so the South Atlantic is a missing link in global biogeography and it is important to define biogeographic boundaries (Copley et al., 2016; Moalic et al., 2012). A further important aspect is the increasing commercial interest in hydrothermal vent sites, because they represent the location of formation of metal-rich seafloor massive sulfide deposits. Slow spreading MOR, such as the Mid-Atlantic Ridge, are expected to bear more than 80% of the known seafloor tonnage of seafloor massive sulfides (German et al., 2016; Hannington et al., 2011; Tivey, 2007).

Since the initial discovery of active hydrothermal vents and sulfide mounds at the axes of MORs in the late 1970s (Corliss et al., 1979; Rona et al., 1986) significant progress has been made in their oceanographic, geological and biological exploration. By mid-2018 the InterRidge Vents Database (Beaulieu et al., 2013) – the authoritative reference for the locations of active hydrothermal vent sites – lists 288 confirmed vent fields and 355 additional sites inferred from water column plume-surveys (Figure 1; Beaulieu, 2015). However, large portions of the global MORs are still unexplored for hydrothermalism (Beaulieu et al., 2015). A prominent example is the Southern Mid-Atlantic Ridge (SMAR) south of 14°S which was, until 2013, a blank spot on the global map of venting (inset in Figure 1).

To better constrain geochemical fluxes related to hydrothermal venting, to define the biogeographic regions of endemic vent communities and to precisely evaluate associated massive sulfide deposits it is essential that we first determine the locations of active vent fields along the SMAR. Inferred vent locations will then serve as the basis for cruise planning and detailed studies of hydrothermalism along the SMAR in the future. In this paper we present the water column results from cruise MSM-25 of RV Maria S. Merian which took place in early 2013 with the primary goal of systematically surveying all ridge segments between 13°-33°S for hydrothermal venting (Devey and cruise-participants, 2013). We combine measurements from 11 dives of an autonomous underwater vehicle (AUV) with those from ship based hydrographic casts. Our approach is based on the detection of several independent tracers for hydrothermal venting: a) the oxidation-reduction potential (ORP), b) turbidity anomalies resulting from hydrothermal particles and c) primordial helium, expressed as  $\delta^3\text{He}$ , discharged into the ocean by vent fluids.

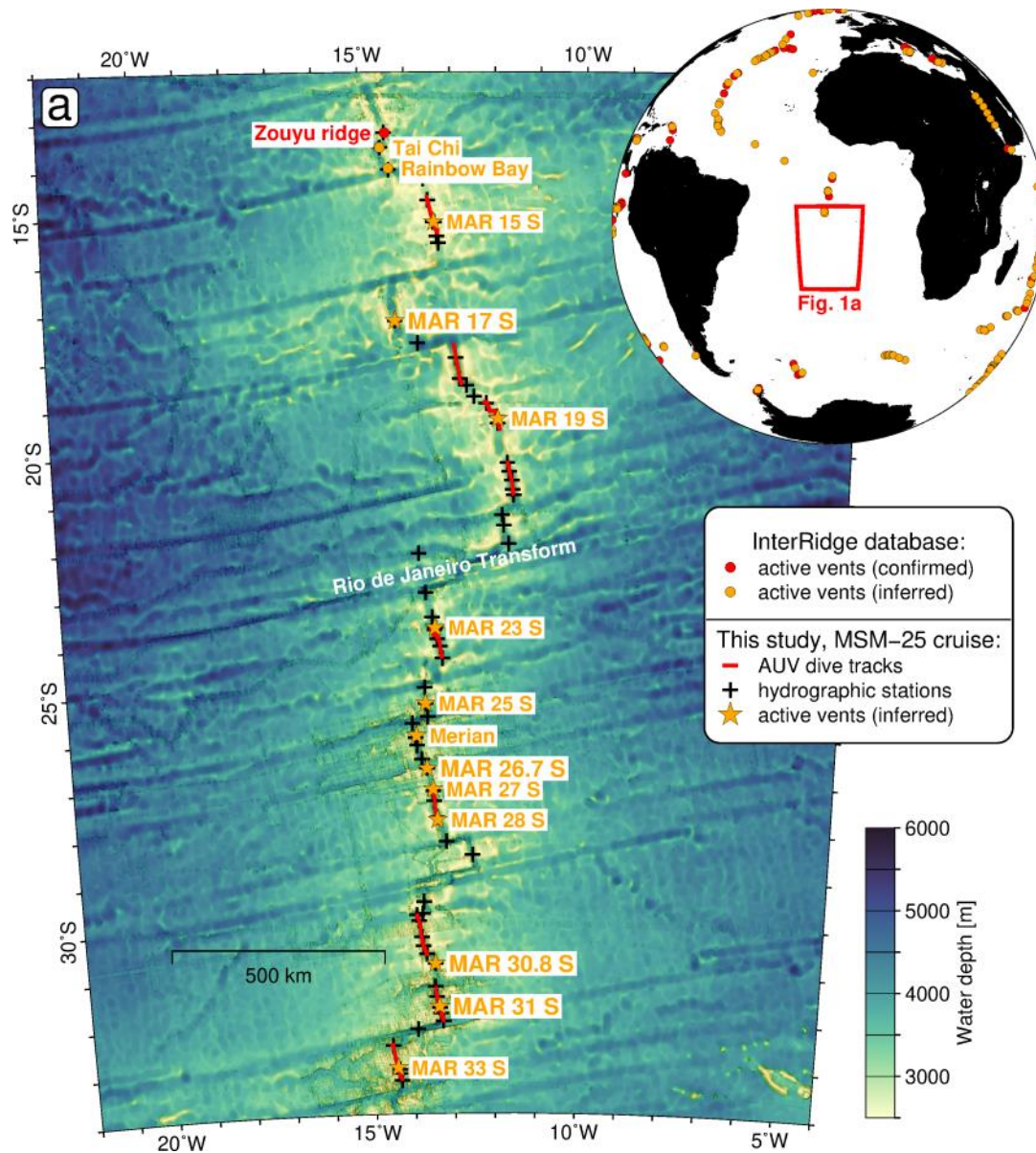


**Figure 1.** Map a, overview of the study area at the Southern Mid-Atlantic Ridge (SMAR) with locations of confirmed (red) and inferred (orange) active vent sites extracted from the InterRidge Vents Database, version 3.4 (<http://vents-data.interridge.org/>). Locations of hydrographic stations and inferred vent sites from the MSM-25 cruise are also given. Bathymetry from GMRT synthesis (Ryan et al., 2009). The globe in the upper right corner shows the location of the bathymetry map and further vent sites from the InterRidge database.

## 2 Hydrothermalism at the Slow Spreading Mid-Atlantic Ridge

With full spreading rates of 20-35 mm a<sup>-1</sup> (DeMets et al., 2010) the Mid-Atlantic Ridge is a slow spreading MOR. Slow spreading MORs make up ~60% of the total MOR system. The compilation of all known vent sites along the global MORs reveals a coincident increase in vent field incidence and spreading rate (Baker et al., 1996; Beaulieu et al., 2015). However, the incidence of vent sites along individual sections of the Mid-Atlantic Ridge is non-uniform and distance between sites varies over an order of magnitude (Beaulieu et al., 2015; German and Parson, 1998). German and Parson (1998) propose these variations are related to larger-scale variations in the interplay between magmatic and tectonic activity along the ridge. In a typical MOR setting, the primary heat source for hydrothermal venting are axial magma chambers, usually beneath the segment center (Baker and German, 2004; German and Parson, 1998). A higher incidence of vent sites along some ridge sections is attributed to deep penetrating faults, which enable heat mining from the lower crust/upper mantle (German and Parson, 1998).

Hydrothermal vents occur in various tectonic settings on the Mid-Atlantic Ridge in diverse lithologies ranging from basaltic hosted, e.g. Turtle Pits near 5°S (Haase et al., 2007), to ultramafic hosted e.g. Ashadze near 13°N (Fouquet et al., 2010). The diversity of host rock lithologies results in diversity in the vent fluid compositions (Edmonds, 2010) and vent faunal communities (Kelley and Shank, 2010). Slow- and ultraslow MORs have the highest diversity of hydrothermal systems of all MORs and since large portions of these ridges are still unexplored they represent highly promising grounds for future discoveries of vent sites with presently unknown characteristics (Baker, 2017; Beaulieu et al., 2015). In contrast to intermediate and fast spreading ridges, where hydrothermalism is limited to the narrow neovolcanic zone, can venting along slow spreading MORs occur far off-axis as in the case of Lost City (~15 km off-axis; Kelley et al., 2001) or the Nibelungen vent field at 8°S (~6 km off-axis; Melchert et al., 2008).

The relative sparsity of active vent sites along slow spreading ridges and the rough morphology make segment-scale tow surveys – as conducted along fast spreading, hydrothermally more active ridges (e.g. Baker et al., 2001; Baker et al., 2017) – very inefficient. Devey et al. (2010) proposed a conceptual model describing the interplay of volcanism, tectonics and hydrothermalism at slow spreading MORs. This model predicts that active venting is most likely to be detected at the magmatically robust axial highs where magma supply is enhanced and on geological time-scales only transiently disrupted by short sequences of tectonic activity. During the MSM-25 cruise we designed our survey strategy in reference to this conceptual model. Focused on morphologically pronounced axial highs, often coinciding with the segment's center and identified from ship-based multibeam bathymetry, the survey program included dedicated AUV dives and/or tow-yo casts to investigate these structures (Devey and cruise-participants, 2013).

## 3 Primordial (Mantle) Helium Emanating from MOR Hydrothermalism

Lupton et al. (1977) were the first to report a massive plume of primordial helium (where the <sup>3</sup>He/<sup>4</sup>He ratio is significantly increased compared to the atmosphere) above the fast spreading East Pacific Rise originating from high-temperature hydrothermal venting. Owing to its inert nature the <sup>3</sup>He concentration in seawater is exclusively altered by dilution making it an ideal tracer for both hydrothermal activity and oceanographic processes (Jean-Baptiste et al., 2008; Lupton, 1998). <sup>3</sup>He anomalies persist over larger distances than particle plumes since the latter may be subject to scavenging, dissolution or particle fallout (Feely et al., 1994; Jean-Baptiste et al., 2008; Lupton and Jenkins, 2017). Plumes of <sup>3</sup>He above the northern Mid-Atlantic Ridge are weak ( $\delta^3\text{He}$  values do not exceed 15% beyond the proximity to vent sites (Jean-Baptiste et al., 2008)). In comparison, at the fast spreading East Pacific Rise an extensive <sup>3</sup>He plume of  $\delta^3\text{He}$  values larger than 50% was observed up to 400 m above the ridge axis (Lupton, 1998). The lower <sup>3</sup>He above the Mid-Atlantic Ridge is due to a lower vent field incidence and the approximately 10 faster renewal rates of Atlantic deep waters than of Pacific deep waters causes an efficient removal of <sup>3</sup>He over the Mid-Atlantic Ridge (Jean-Baptiste et al., 2008).

Surveys of  $^3\text{He}$  have been successfully used to trace hydrothermal activity at regional and local scales on slow spreading MORs (Jean-Baptiste et al., 2004; Jean-Baptiste et al., 2008; Jean-baptiste et al., 1991). The discharge of  $^3\text{He}$  at the Mid-Atlantic Ridge is strongest at high-temperature magmatic-hosted hydrothermal systems and generally weaker at, low-temperature cumulate- or mantle-hosted systems, e.g. Lost City and Ashadze (Charlou et al., 1998; Edmonds, 2010; Jean-Baptiste et al., 2008; Keir et al., 2006). First indications for active venting along the southern MAR came from large scale  $^3\text{He}$  distributions obtained on sections World Ocean Circulation Experiment (Rüth et al., 2000), where  $^3\text{He}$  far field plume signals emanating from the ridge crest were observed between 11°S and 30°S.

## 4 Materials and Methods

### 4.1 Ship and AUV Based Plume Surveying

We deployed five Pacific Marine Environmental Laboratory (PMEL) Miniature Autonomous Plume Recorders (MAPRs) equipped with turbidity, oxidation-reduction potential (ORP), temperature and pressure sensors. For standard vertical casts one MAPR unit was mounted to the SeaBird Electronics 911plus conductivity-temperature-depth (CTD) probe. For tow-yo stations additional MAPR units were mounted on the cable roughly 50, 100, 150 and 200 m above the CTD. The MAPR turbidity sensor is a custom built, high-sensitivity optical backscatter sensor (Seapoint Sensors, Inc) that is specifically tuned to identify plumes of hydrothermal particles, typically discharged by hydrothermal vents of exit temperatures  $> 100^\circ\text{C}$  (Baker et al., 2016). Turbidity is measured in dimensionless nephelometric turbidity units (NTU) and reported here as the anomaly ( $\Delta\text{NTU}$ ) above ambient background seawater. ORP anomalies are caused by nanomolar concentrations of reduced hydrothermal chemicals (e.g.  $\text{Fe}^{2+}$ ,  $\text{HS}^-$ ,  $\text{H}_2$ ) which are rapidly oxidized or metabolized after being discharged into the ocean (Walker et al., 2007). ORP anomalies typically occur closer to the vent site than turbidity anomalies and thus are a good indicator of active venting within  $\sim 1\text{-}2$  km (Baker et al., 2016; Baker et al., 2017). The ORP sensor response is characterized by a steep decrease in potential once a plume anomaly is intersected, followed by a gradual recovery (Baker et al., 2016). Absolute potential values,  $E$ , given by the ORP sensor may vary between individual sensors due to sensor drift or hysteresis. Therefore, the time derivative  $dE/dt$  is used to define an ORP anomaly ( $\Delta E$ ) whenever  $dE/dt$  is more negative than  $-0.02$  mV for consecutive measurements and the total drop in voltage is  $> 1.0$  mV. By applying these thresholds we avoid ambiguous signals caused by the variable nature of the background values. The AUV was also equipped with turbidity and ORP sensors.

During the MSM-25 cruise we conducted hydrographic casts at all high-relief segment centers identified from topography and additional casts at segment-ends of all 16 first-order ridge segments between 13-33°S. The AUV accomplished nine long-range missions during which the vehicle was programmed to survey at 150 m altitude and two dedicated dives above the Zouyu Ridge (13°S) and the Merian vent field (26°S) were carried out at 50 m altitude.

### 4.2 Sampling and Analysis of Helium Isotopes

For the analysis of helium isotopes in the waters above the SMAR two different sampling methods were used (Devey and cruise-participants, 2013). 522 samples were filled into pinched-off copper tubes that were sealed free of head space and 451 samples were drawn into evacuated glass ampoules by leaving a head space for gas phases, following the methodology of Roether et al. (2013). After the cruise all samples were further processed and analysed in the Bremen Helium Isotope Laboratory (Helis; Sültenfuß et al., 2009). After gas extraction (only necessary for copper tube samples) the gases are analysed with a fully automated mass spectrometry facility, of which the technical details are provided in Sültenfuß et al. (2009). 973 samples were successfully analysed and the achieved noble gas dataset (including concentrations of  $^3\text{H}$ ,  $^4\text{He}$ , Ne) was carefully checked for spurious values, by also considering neon. We discard all samples that show a  $\Delta(\text{Ne})$  value lower than 1% and higher than 8% as values

outside this range are implausible (Well and Roether, 2003). The neon data were further used to correct for excess air in the samples caused by wave induced bubble injection, melting ice or contamination, following the approach of (Roether et al., 2001); Roether et al. (1998). Details of excess air correction are provided in Supporting Information Texts S1-S3. In the following we present helium data as excess air corrected values in the commonly used delta notation,  $\delta^3He = \left(\frac{R}{R_a} - 1\right) 100$ , where  $R$  is the  $^3He/^4He$  ratio in the sample and  $R_a$  is the  $^3He/^4He$  ratio in the atmosphere.

### 4.3 Bathymetry Data and Underwater Positioning

Bathymetric data were acquired with a hull-mounted Kongsberg EM122 echosounder. The raw data were manually cleansed of outliers and grids of 50 m horizontal resolution were produced for each surveyed ridge segment. Wherever available, the bathymetry grids were supplemented with auxiliary ship-based data from the Global Multi-Resolution Topography Synthesis archive (Ryan et al., 2009). A hull-mounted ultra-short baseline system (USBL, IXSEA “Posidonia”) was used for precise positioning of the CTD rosette and MAPRs during tow-yo stations. The AUV operated during the cruise (GEOMAR’s REMUS 6000 vehicle “ABYSS”) is equipped with an inertial navigation system and a USBL beacon. The inertial navigation system gives relative positions during the dive while the USBL allowed us to determine the vehicles absolute position whenever the ship was in proximity during the dives. For each dive at least two independent USBL position fixes (typically when the AUV had arrived at the bottom and at a later stage before the vehicle departed from the bottom) were achieved (Devey and cruise-participants, 2013). Using these fixes, the horizontal drift of the inertial navigation system was determined and yielded deviations within 100–900 meters after a 12-18 h dive. The AUV navigation data was shifted accordingly in post processing.

### 4.4 Current Velocity Measurements and Predicted Barotropic Tidal Velocities

Current velocities were measured with two RDI Workhorse lowered Acoustic Doppler Current Profilers, mounted to the CTD-rosette water sampler (Devey and cruise-participants, 2013). One sensor faced downwards and the second one upwards and both instruments were operated in synchronous mode, recording average velocities in 10 m vertical bins. The current velocity data were processed following the scheme of Visbeck (2002). In this study we only use measurements from near the seafloor (less than 300 m above bottom), gathered via the instruments bottom-tracking mode. The amplitudes and directions of predicted barotropic tidal velocities for the location and the operation period of selected CTD stations were retrieved from the global model of ocean tides prediction, TPXO7.1, developed by Egbert and Erofeeva (2002).

## 5 Results and Discussion

### 5.1 $^3He$ above the SMAR axis

The analysis and quality control of noble gas data yielded 525 discrete  $\delta^3He$  values above the SMAR axis (Figure 2), which is unprecedented in its extent along the spreading axis and density of sampling in the bottom waters.  $\delta^3He$  ranges between -3.4 % and 146.9 % with negative values only present at depths shallower than 2000 m (Figure 2b) and values > 10 % only occurring at discrete sites deeper than 2000 m (Figure 2a). The general pattern of  $\delta^3He$  values above the SMAR suggests that the oceanic background in the different water masses does not exceed 10 % and all values above this threshold may thus be considered affected by hydrothermal input (Figure 2). Our meridional transect of background  $\delta^3He$  (omitting all values of  $\delta^3He > 10$  %, Figure 2b) is in agreement with the cross-cutting zonal transects of  $\delta^3He$  at 19°S and 30°S presented in Roether et al., (1998) and R uth et al., (2000). The zonal section at 19°S shows a  $\delta^3He$  maximum of 5.5% directly above the SMAR axial seafloor and ~2000 m depth (R uth et al., 2000) which is consistent with our dataset (Figure 2b). The zonal section at 30°S shows a slightly stronger maximum of 7% that reaches from the seafloor up to 1000 m depth and so does



our data (Figure 2b; R uth et al., 2000). Overall, the  $^3\text{He}$  values are similar with those above the Northern Mid-Atlantic Ridge and lower than those above the fast Spreading East Pacific Rise (Lupton, 1998).

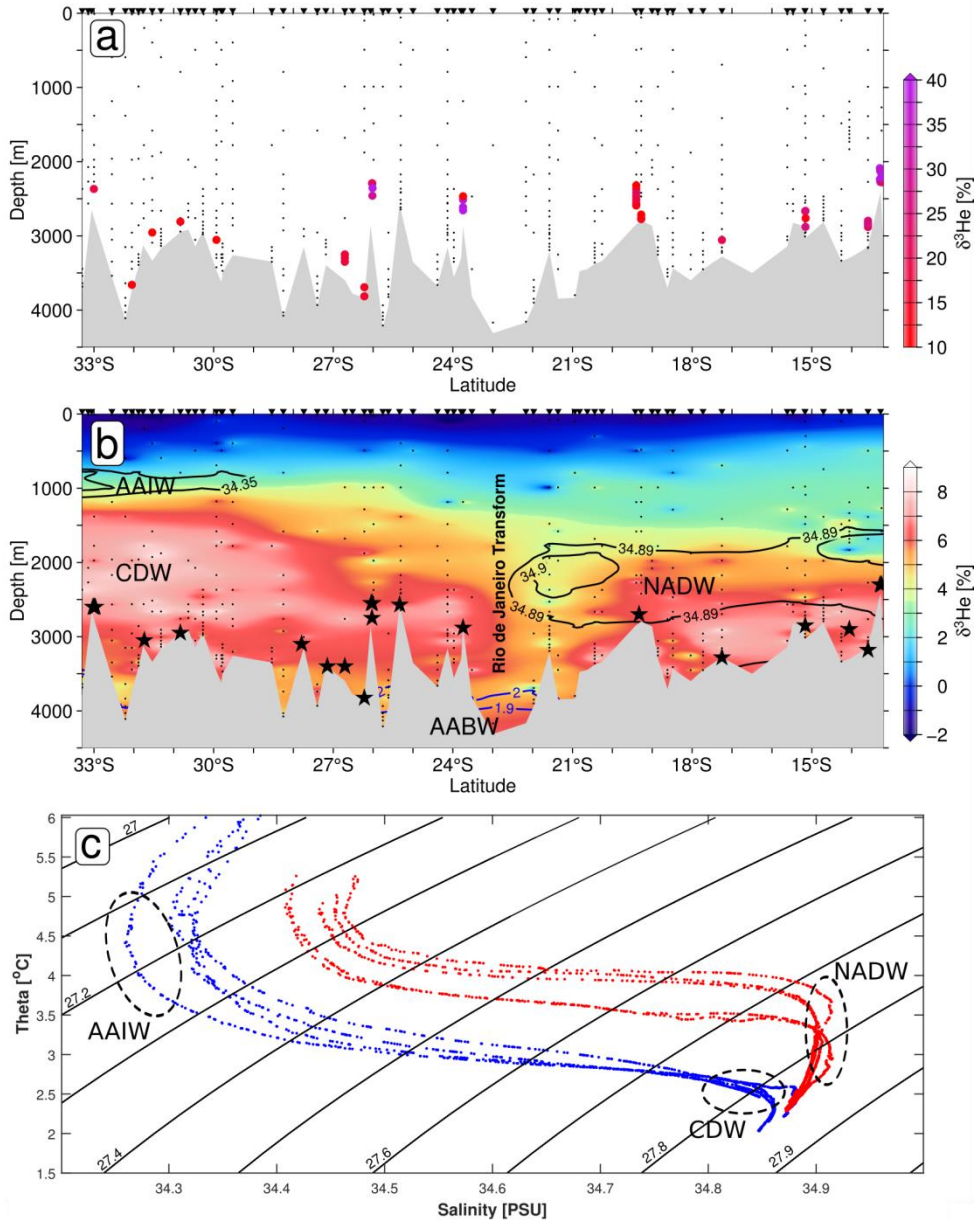


**Figure 2.** Two aspects of the  $^3\text{He}$  distribution above the SMAR. Panel a shows samples as colored circles where  $\delta^3\text{He}$  is larger than 10%, which are considered as hydrothermally sourced anomalies. Small black dots show all sampling locations that yielded reliable  $\delta^3\text{He}$  values after quality control. Panel b shows a gridded meridional section  $\delta^3\text{He}$ . Values of  $\delta^3\text{He} < 9\%$  have been omitted from gridding and thus the image represents the oceanic background in  $^3\text{He}$ , which is not immediately affected by hydrothermalism. Black contours delineate salinities  $> 34.89$  psu, indicative of North Atlantic Deep Water (NADW). Blue contours delineate Antarctic Bottom Waters (AABW) of potential temperatures  $< 2.0$  °C. CDW denotes Circumpolar Deep Waters carrying excess  $\delta^3\text{He}$  from the Pacific. Black stars indicate locations of identified hydrothermal vent sites. Panel c, T-S diagram for stations south of the Rio de Janeiro Transform (blue) and stations north of the Transform (red). Contours represent isopycnals. Data shallower than 700

*dbar have been omitted. Note, that different water masses of AAIW, NADW and CDW occupy distinct temperature and salinity ranges.*

## **5.2 Is the Rio de Janeiro Transform (22°S) a Barrier to the Meridional Dispersal of Vent Fauna?**

The Rio de Janeiro Fracture Transform valley at 22°S represents the deepest cross-passage in the survey area and is associated with a ~220 km offset in the ridge axis. The fracture zone coincides with a gap in the distribution of hydrothermal vent fields between 19°S - 23°S and is marked by a decrease of <sup>3</sup>He concentrations throughout the water column (Figure 2b). Our hydrographic data from the SMAR axis indicate that the southward progression of North Atlantic Deep Waters (NADW) is interrupted above this region (Figure 2b,c). Waters at 1000-2500 m depth in the region south of 27°S represent Circumpolar Deep Waters (CDW) that are enriched in <sup>3</sup>He ( $\delta^3\text{He} > 6\%$ ) due to the elevated <sup>3</sup>He background from the Pacific entering the South Atlantic via the Drake Passage (Rüth et al., 2000; Well et al., 2003). Mercier et al. (2000) report a throughflow in the Rio de Janeiro Transform supplied by cold and fresh bottom waters from the deep basins west of the SMAR. This is supported by our hydrographic measurements revealing Antarctic Bottom Waters (AABW) identifiable from potential temperatures < 2.0 °C (Broecker et al., 1976) in the deepest part of the transform valley (Figure 2b).

The along-axis dispersal success of passive larvae and microbes endemic to hydrothermal vents is dependent on bottom currents and the frequency of vent sites (McGillicuddy et al., 2010; Mullineaux et al., 2002). The crossflowing waters and the absence of active vents in the 19°-23°S region prevent the meridional dispersal of vent endemic larvae. The maximum southward progression of NADW suggests that larvae from the northern and Equatorial MAR may not be transported further south than the Rio de Janeiro Fracture Zone. We hypothesize that the topographic controlled hydrography and the sparse distribution of active vents in the 19°-22°S region constitute a physical barrier to the meridional dispersal and genetic connectivity between the different vent fauna communities found along northern MAR and the Circum-Antarctic Ridges (Copley et al., 2016; Moalic et al., 2012). However, this hypothesis may only be validated by biological investigations of the vent fauna immediately north and south of the Rio de Janeiro Transform.

## **5.3 Detailed description of individual plume sites**

The following section describes in detail the individual plumes observed in geographical order from north to south. We also discuss the locations of underlying vent sites and their tectonic setting. A comprehensive summary of the coordinates of all the vent sites is provided in Table 1.

### **5.3.1 Zouyu Ridge, 13°16'S**

The unusually extensive axial volcanic high near 13°16'S (Zouyu Ridge) was targeted by one AUV mission at 50 m altitude and tow-yo station 124 (Figure 3a, b). The axial high measures approximately 20 km along-axis by 8 km across-axis and rises as high as the local rift flanks (Figure 3a, b). Tow-yo 124 started at the western rim of the axial high and after pursuing a southeasterly heading for 3 km the course was altered to north and the CTD was towed across a N-S oriented chain of up to 100 m high mounds sitting on top of a linear scarp (possibly fault or volcanic fissure; Figure 3b). The S-N oriented limb of the tow-yo crossed the previously known Zouyu-2 vent field (Figure 3b, e; Tao et al., 2011; Tao et al., 2017). The CTD sensor encountered a buoyant hydrothermal plume ~1 km south of the Zouyu-2 location (at 13°17.31'S/14°24.59'W; Figure 3e, f) marked by a temperature anomaly of +0.31 °C and strong density inversions between 2165-2210 m depth (Figure 3f).

An extensive neutrally buoyant plume was observed at ~200 m above the seafloor (Figure 3d, e). The plume increases slightly in vertical extent at the northern end of tow-yo 124, possibly due to venting near the Zouyu-1 vent field (Figure 3b). Increased turbidity in the bottom waters near the southern apex of the tow-yo is consistent in both, MAPR and AUV data (Figure 3b, d-e) and may indicate the presence of

several active chimneys near the identified buoyant plume. Widespread ORP anomalies were observed in the upper part of the particle plume, ~50 m above the layer of highest turbidity (Figure 3d, e). Occasional ORP anomalies were also observed below the particle plume, above the Zouyu-2 site, in the buoyant plume and near the western rim of the axial high (Figure 3d, e). The stratification above the axial high shows a staircase pattern as indicated by the variable spacing of isopycnals (Figure 3d, e and Supporting Information Figure S2) and the shape of the density profile in Figure 3f at depths shallower than 2160 m. Water samples along the tow-yo track yielded  $\delta^3\text{He}$  values of 22.9-47.9 ‰ in the neutrally buoyant plume and an exceptionally high value of 146.9 ‰ in bottle number 6 directly above the buoyant plume (Figure 3e, f). Average current velocities in the near bottom layers range from 5–17  $\text{cm s}^{-1}$  and show a gradual change in direction along the tow-yo track, i.e. through time of measurement (Figure 3c). Predicted barotropic tidal velocities for this region, at the time of tow-yo operations, range from 3-5  $\text{cm s}^{-1}$  and show a gradual change in direction coinciding with measured near-bottom current velocities (Figure 3c).

The coordinates of Zouyu-2 from Tao et al. (2011), do not refer to an active vent but give the dredging location of a chimney fragment. Based on tow-camera observations Tao et al. (2011) estimated the vent field to have an extent of ~1 km in the N-S direction which suggests the hydrothermal discoveries of Tao et al. (2011) in 2009/2011 and the buoyant plume we discovered in 2013 relate to the same vent field, Zouyu-2. ORP signals are indicative of recently discharged hydrothermal fluids (Walker et al., 2007), suggesting the neutrally buoyant plume is particularly ‘fresh’ in its uppermost layers (Figure 3d, e). The current velocity measurements suggest that tides rapidly spread the plume waters across the axial high. Similar types of advection of hydrothermal plumes by tides and background currents have been described at other sites on the MAR, such as above the Logachev vent field (Schmale et al., 2012) or the Nibelungen vent field (Walter et al., 2010).

A constant vertical offset between an ORP plume and a particle plume is unusual and has never before been observed above any active vent site in such clarity. As the number of active vent sites on the Zouyu Ridge and their chemistries are unknown we can only speculate about the cause of this vertical offset. We present two scenarios to explain this offset. In the first scenario, the Zouyu-2 vent field is the primary source of the neutrally buoyant plume and the upper layer of anomalous ORP and low turbidity represents the freshest portion of the plume while the lower layer of highest turbidity and without ORP signal is composed of mature plume waters. Such a layering could be sustained by gravitational separation of hydrothermal particles from the reduced chemicals (e.g.  $\text{Fe}^{2+}$ ,  $\text{HS}^-$ ,  $\text{H}_2$  producing the ORP signal) supported by the staircase stratification. The settling of particles is retarded by a jump in density (crossing the 36.992  $\text{kg m}^{-3}$  isopycnal, Figure 3d-f and Supporting Information Figure S1). The vertical offset may also result from overshooting of the buoyant plume waters in the wake of which particles fall back to a level of higher density than the reduced chemicals. In the second scenario, the neutrally buoyant plume is fed by two separate venting sites of different characteristics. Site A (possibly the one producing the buoyant plume) discharges particle-rich fluids that are poor in reduced chemicals and thus produce no ORP anomalies beyond the buoyant plume. Site B is rich in reduced chemicals, poorer in particles and either located at shallower depths (possibly on one of the ~100 m high mounds) or has higher exit temperatures than site A in order to produce a plume of ~50 m higher rise height.

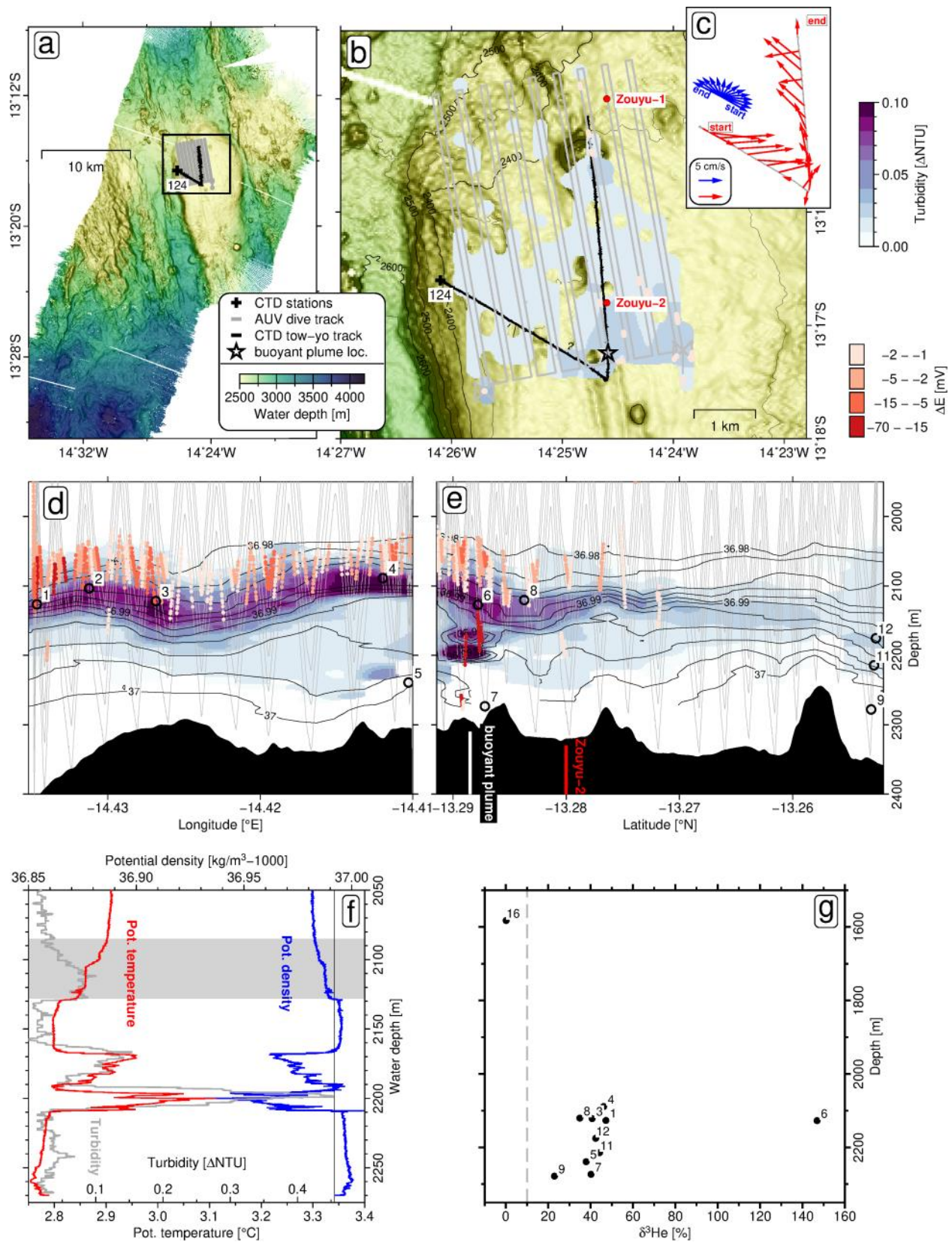


**Figure 3.** Plume results from the Zouyu Ridge. Panel a, bathymetry overview of the segment. The black rectangle indicates perimeter of map b. Detailed map b shows the flat-topped axial high

hosting the Zouyou-1 and 2 vent fields, coordinates from Tao et al. (2017). The gray shading represents gridded AUV turbidity, at the same color scale as MAPR data in panels d and e. Note, the AUV was flown at 50 m above seafloor and thus remained below the main turbidity plume. Panel c, vectors of measured current velocities, red, along the tow-yo track and predicted barotropic tidal current velocities, blue. Panels d and e show results from tow-yo station 124 separately for the NE-SW and S-N striking parts of the station, respectively (tow track is plotted on map b). Faint gray lines indicate MAPR tracks, blue shading scales with turbidity, red dots show  $\Delta E$  anomalies. Numbered circles show water sampling locations and black contours are isopycnals calculated from CTD data. Panel f, profiles of temperature, density and turbidity of the CTD sensor for the tow-yo up-cast crossing the buoyant plume. To correct for a delayed response of the CTD-mounted turbidity sensor, the signal was shifted 3 m upwards before plotting. The gray shaded area indicates the depth of the neutrally buoyant particle plume and the vertical black line shows the  $36.992 \text{ kg m}^{-3}$  isopycnal, coinciding with the lower boundary of the particle plume. Panel g,  $\delta^3\text{He}$  results from station 124 with labels corresponding to bottle numbers in panels d and e.

### 5.3.2 Tai Chi Vent Field, 13°36'S

Vertical CTD station 122 above the previously known Tai Chi vent field (also spelled Taiji; Figure 4a) located at approximately 3100 m water depth on the northern face of an inside corner high marking the southern boundary of a non-transform ridge-offset (Li et al., 2018). Turbidity and ORP anomalies were found between 2810 – 2950 m depth (Figure 4b). The upper boundary of the plume is sharply defined and correlates with a maximum  $\delta^3\text{He}$  value of 29.5 ‰ (Figure 4c). Li et al. (2018) reported a weak temperature anomaly at 3000-3050 m depth, above the vent field in 2011. Their camera surveys did not find sites of active discharge, leading to the conclusion that only diffusive venting was present in 2011. However, our discovery of a plume rich in  $^3\text{He}$ , particles and of reduced ORP ~200 m higher suggests that considerable, high-temperature venting was present in 2013.

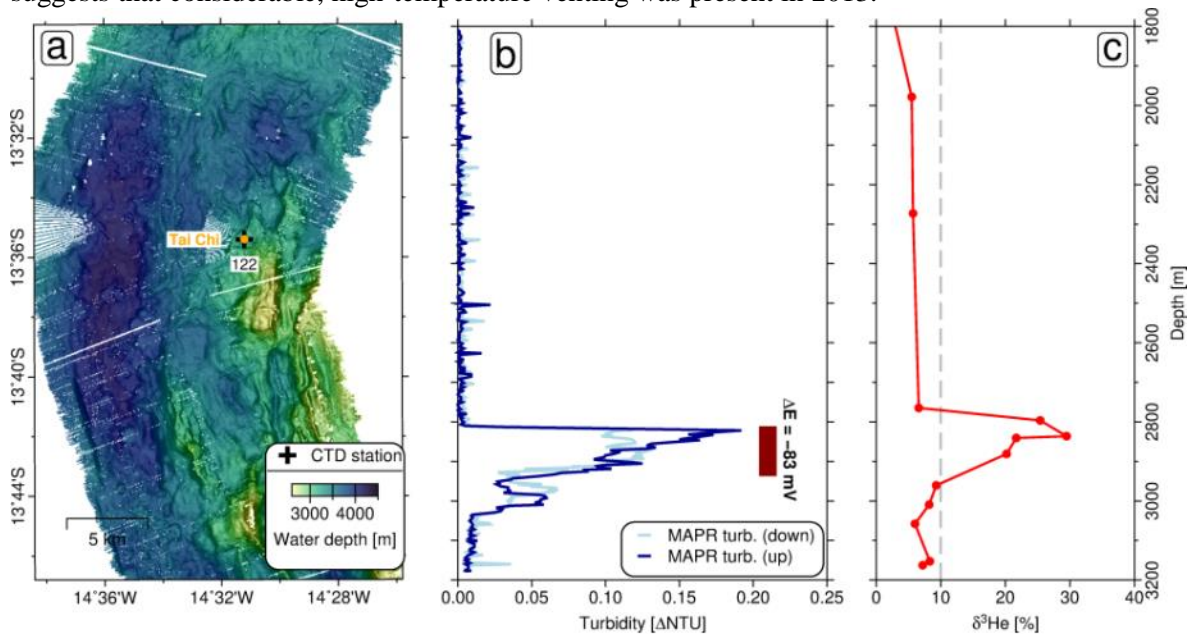


**Figure 4.** Results from the Tai Chi vent field. Bathymetry map a shows the location of the Tai Chi vent field above which CTD station 122 was located. Panel b, MAPR turbidity and  $\Delta E$  anomalies (red bar) at station 122. Panel c, vertical profile of  $\delta^3\text{He}$  at station 122.

### 5.3.3 Deyin-1 Vent Field, MAR 15°10'S

The 14°6'S - 15°30'S segment was investigated by a long-range AUV mission which revealed turbidity and ORP anomalies around 15°9.97'S/13°21.34'W and subsequently this site was further investigated by tow-yo station 116 (Figure 5). In 2011 a plume had been observed at the same site by a Chinese hydrothermal survey (S Wang et al., 2017) although this was unpublished at the time of the MSM-25 cruise. The site is located on a ~200 m high neovolcanic ridge in the center of the axial valley which was crossed from east to west by tow-yo 116 (Figure 5a, b). We mapped a particle plume at 2440-2800 m depth extending to east and west of the neovolcanic ridge (Figure 5e). An ORP anomaly was exclusively detected to the west, suggesting the active vent field is located on this side at ~ 2850 m depth. Water samples 2 and 4 (Figure 5e, f) collected within the particle plume yield  $\delta^3\text{He}$  values of 25.9 ‰ and waters from slightly outside the particle plume (bottle numbers 5,7) fall back to the oceanic background (Figure 5e). None of the monitored hydrothermal tracers showed an anomaly at the nearby station 113, implying that this plume is locally confined. Dredged rock samples from this site yielded basalts and massive sulfides (H Wang et al., 2017).

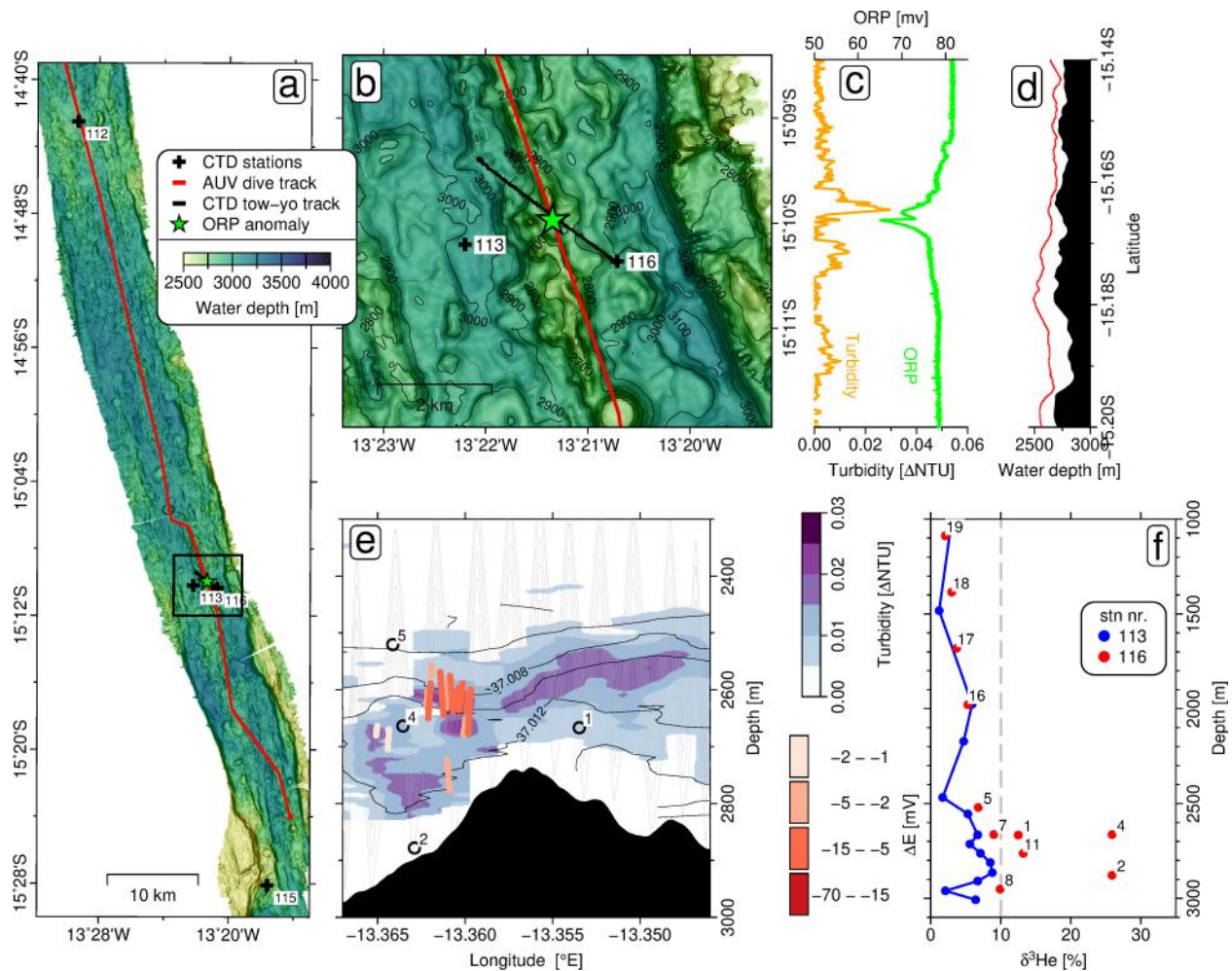


**Figure 5.** Results from the Deyin-1 site. Map a, bathymetry of the segment with black frame indicating the perimeter of map b. Panel c, turbidity and ORP measured along the AUV track on map b, plotted versus latitude. Panel d shows vehicle and seafloor depths versus latitude. Panel e, results from tow-yo station 116 with faint gray lines indicating MAPR tracks, blue shading representing turbidity and red dots showing  $\Delta E$  anomalies. Numbered circles show water sampling locations and black contours are isopycnals. Panel f,  $\delta^3\text{He}$  results from station 113 and

116 with labels corresponding to bottle numbers in panel e. Note, nearby CTD cast 113 did not see any hydrothermal anomaly.

### 5.3.4 MAR 17° S

The segment between 16°24'S and 17°36'S was sampled by vertical CTD station 107, located above an axial high at the segment center. There, the axial valley is unusually narrow, 1.5 km wide, compared to ~10 km width further north and south (Figure 6a). An  $\Delta E$  anomaly of -21 mV was detected between 3010 and 3015 m depth (~260 m above the seafloor) but no significant increase in turbidity was observed (Figure 6b). One water sample from 3055 m depth yielded a  $\delta^3\text{He}$  value of 19.9 ‰ confirming the presence of hydrothermal input in the area (Figure 6c). The ORP anomaly implies that the source is not far (< 1 km) from the sampling site and the absence of a turbidity anomaly suggests that venting is likely of low-temperature and particle-poor character.

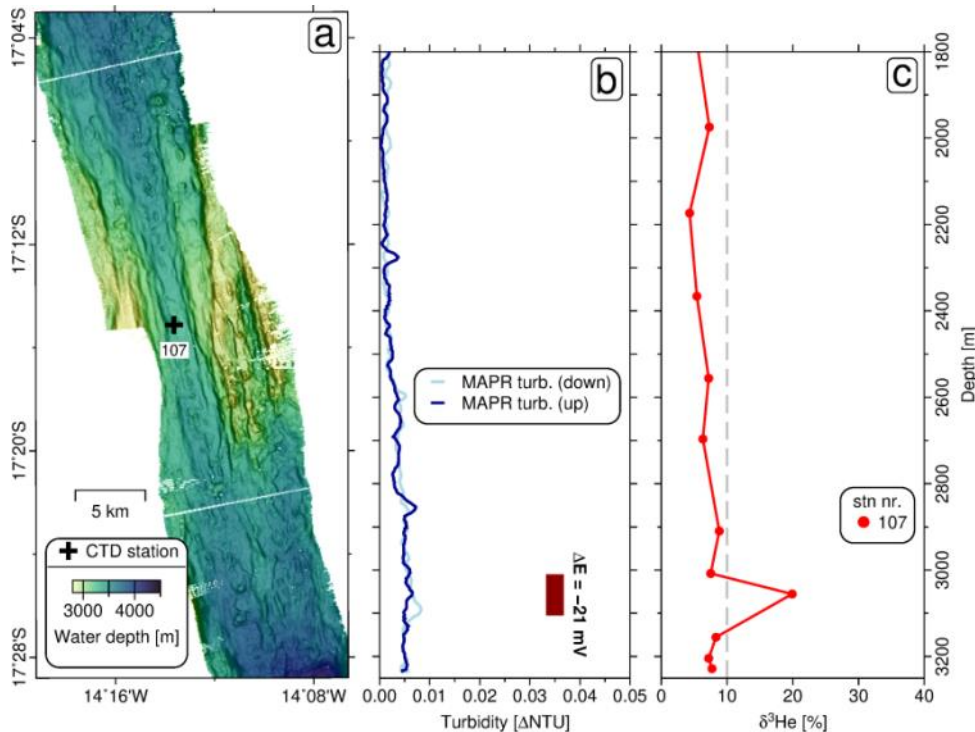


**Figure 6.** Results from the 17°S plume site. Map a, bathymetry map with location of CTD 10. Panel b, turbidity and depth of  $\Delta E$  anomaly at station 107. Panel c, profile of  $\delta^3\text{He}$  for station 107.

### 5.3.5 MAR 19° S

The SMAR axis between 19°S and 19°36'S, comprising several second-order ridge segments, was surveyed by one long-range AUV mission and three vertical CTD casts. In this region the ridge axis is characterized by a ~5 km wide axial valley that is, in most places, not significantly deeper than the ridge flanks and bears numerous volcanic mounds (Figure 7a). During the AUV mission a 0.08  $\Delta\text{NTU}$  turbidity anomaly was observed near 19°20.82'S/11°56.4'W in 2470 m water depth (Figure 7a-c) and an ORP anomaly of -20 mV was observed at 19°19.8'S/11°56.52'W in 2585 m water depth, approximately 1.2 km north of the turbidity anomaly. No turbidity or ORP anomalies were detected at tow-yo station 102 (~10 km south of the AUV ORP anomaly) and CTD cast 103 (~6 km north of the AUV ORP anomaly). However, at both sites the  $\delta^3\text{He}$  values exceeds the oceanographic background with the highest value of 22.8 ‰ occurring at 2420 m water depth at station 102 (Figure 7d).

Most of the anomalies can be explained by the presence of a single hydrothermal field and predominantly southwards directed currents in the area. The vent field's potential location is near the maximum ORP anomaly, with the neutrally buoyant plume spreading at water depth between 2400 and 2600 m, where the maxima in turbidity and  $\delta^3\text{He}$  occur. Background  $\delta^3\text{He}$  values in the 2400-2600 m depth interval at station 103 (Figure 7d) support the hypothesis that the plume is mainly dispersed to the south and the minor  $\delta^3\text{He}$  anomaly below 2700 m depth at this site may indicate another hydrothermal plume.

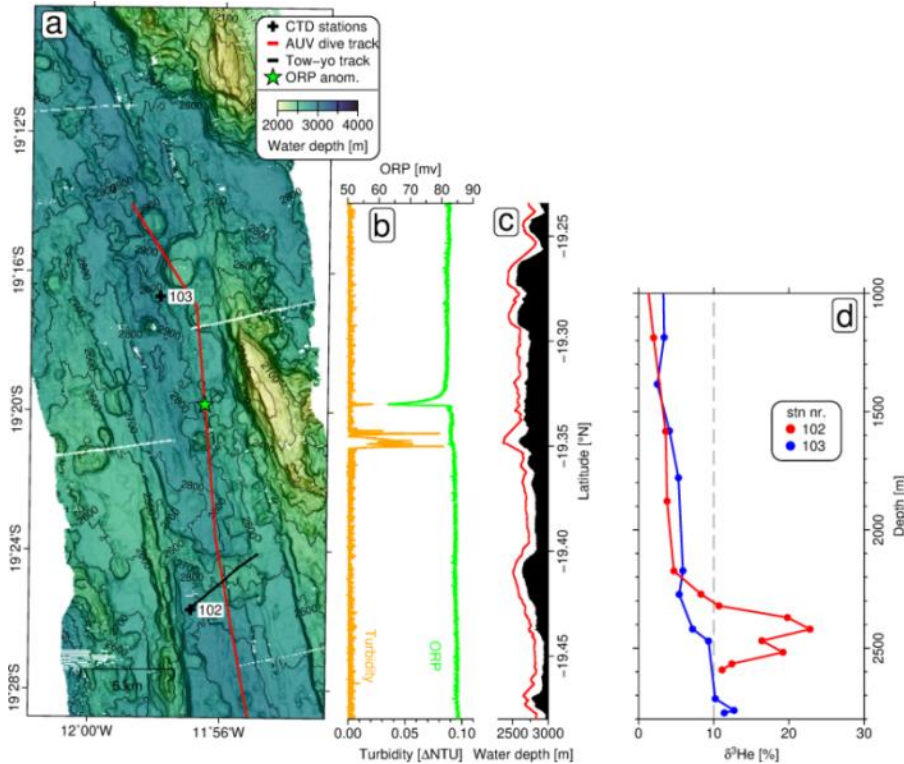


**Figure 7.** Results from the MAR 19° S site. Panel a, bathymetry with AUV track and station locations. Panel b, turbidity and ORP versus latitude along the AUV track plotted in a. Panel c, vehicle and seafloor depths versus latitude along the AUV track. Panel d, vertical profiles of  $\delta^3\text{He}$  for stations 102 and 103.

### 5.3.6 MAR 23° S

The 22°54'S - 24°24'S segment was surveyed by five vertical CTD casts, one tow-yo and one long-range AUV dive, which zigzagged across the axial valley from north to south (Figure 8a). A plume was discovered near the start of the AUV mission (Figure 8a). The ridge axis in this region is defined by the (to date) southernmost known oceanic core complex (OCC) on the Mid-Atlantic Ridge. This OCC exhibits typical ridge-perpendicular corrugations and measures ~16 km along strike. The OCC rises high above the surrounding axial valley floor and large rider blocks (or volcanic ridges) sitting on top, mostly on its northern part (Figure 8a). The strongest ORP signal was detected on top of the detachment fault surface, about 1.5 km east of the hanging-wall cut-off and in proximity to a topographic feature, possibly a rider block or volcanic ridge (Figure 8b). Tow-yo station 70 was towed in a W→E direction and the MAPR data revealed a particle plume between 2500 and 2700 m depth (Figure 8e) that is coincident with ORP anomalies of up to -61 mV near the western end of the tow-yo track (near 23°44.68'S/13°23.59'W) indicating the location of the vent field which is ~6 km E off the ridge axis (Figure 8a, b). Water samples collected ~1 km east of the strongest ORP anomaly show high  $\delta^3\text{He}$  values up to 42.4 % within the particle plume (bottles 5,6,8 in Figure 8f).



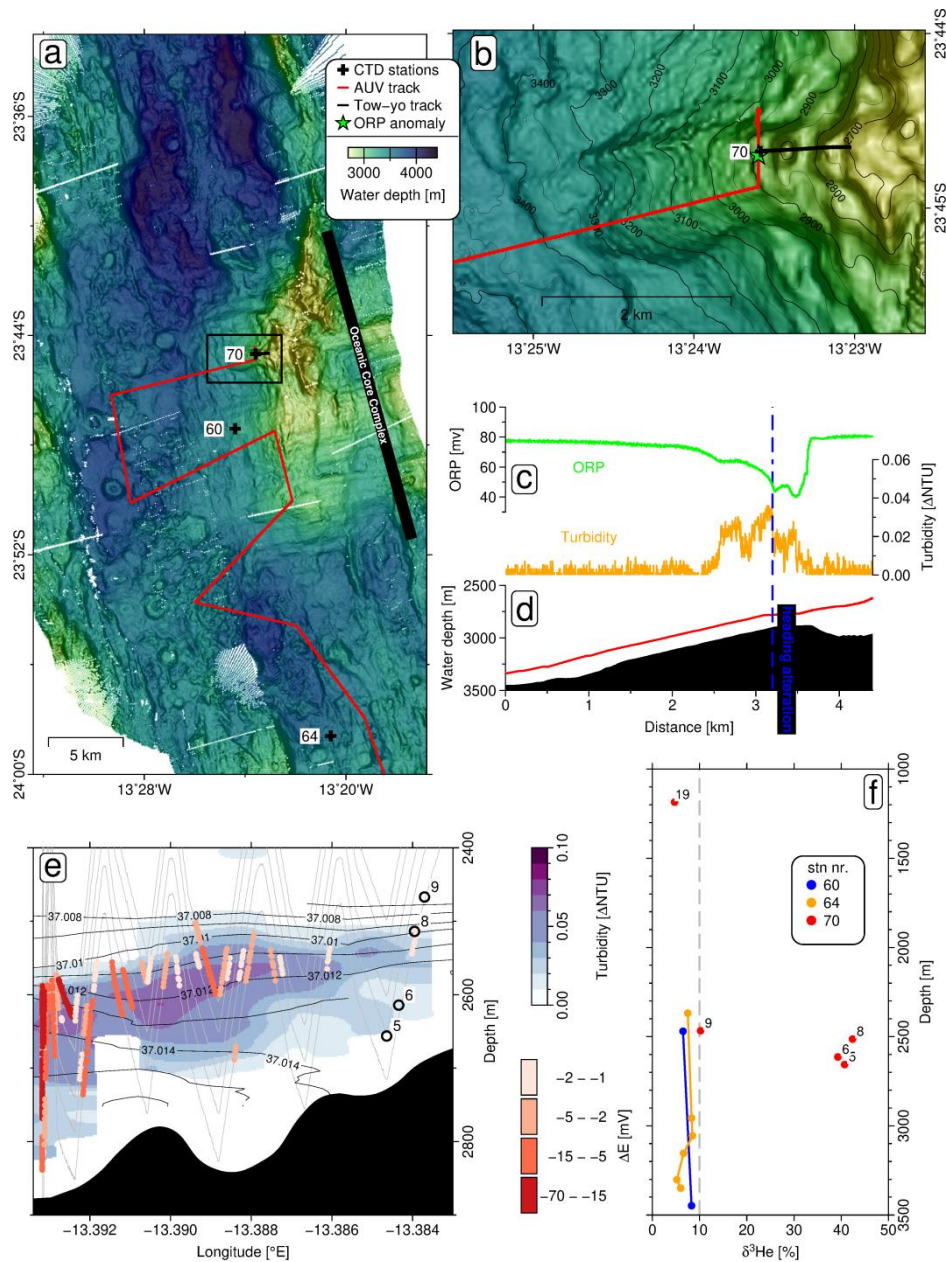


**Figure 8.** Results from the 23°S segment. Map a provides an overview of the ridge segment with black bar roughly indicating the N-S extend of the oceanic core complex. The black frame indicates the perimeter of map b. Map b shows a sub-section of the AUV track in vicinity of the discovered plume. Panel c shows AUV turbidity and ORP data measured along the track section displayed in map b. Panel d indicates the vehicle and seafloor depths along the track section displayed in map b. The vertical dashed blue line indicates where the AUV altered its heading. Note, the AUV was diving from north to southwest and the location where heading was altered is indicated by the vertical dashed line. Panel e, results from tow-yo station 70 with faint gray lines indicating MAPR tracks, the blue shading representing turbidity and colored red dots showing ORP anomalies. Numbered circles show water sampling locations and black contours are isopycnals calculated from CTD data. Panel f,  $\delta^3\text{He}$  profiles of stations 60, 64 and 70 with labels corresponding to bottle numbers of station 70 in panel e.

### 5.3.7 MAR 25° S

The 24°56'S – 25°36'S segment was investigated by two vertical CTD casts (52, 56) and tow-yo station 54 above the generally smooth-topped axial high at the center of the segment (Figure 9a). ORP anomalies up to -31 mV were detected in the first 100 m above the seafloor, near the start of the tow-yo (around 25°20.10'S/13° 37.83'W; Figure 9b, c) indicating the potential vent site location. A weak increase in turbidity rising ~220 m above the seafloor was detected ~1 km north of the ORP anomalies (Figure 9c). No turbidity or ORP anomalies were detected on the W→E trending portion of the tow-yo cast and the  $\delta^3\text{He}$  values from the western end of the tow-yo station, did not exceed the oceanic background (Figure 9d). Since the water samples stem from distances further than 4 km from the ORP signal, it cannot be ruled out that this vent site discharges minor amounts of  $^3\text{He}$ .

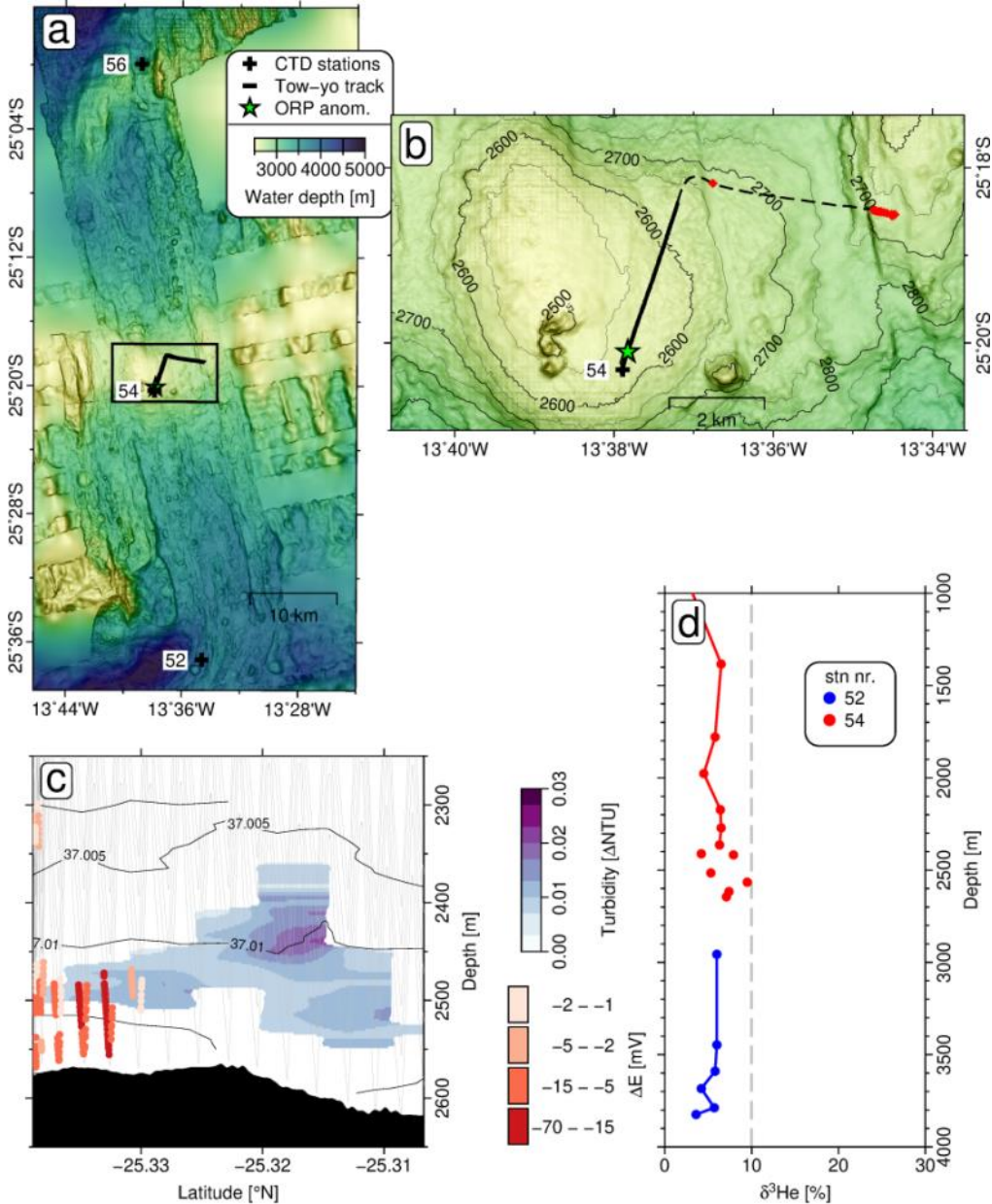


**Figure 9.** Results from the 25°S plume site. Map a, bathymetry of the ridge segment with the black frame indicating the perimeter of map b. Red diamonds on map b indicate locations of water sampling, used for helium analysis. Panel c, results from the S→N trending portion of tow-

yo station 54 (track shown on map b) with blue shading representing turbidity and red dots showing  $\Delta E$  anomalies. Panel d,  $\delta^3\text{He}$  profiles of stations 52 and 54.

### 5.3.8 Merian Vent Field (26°S)

The 25°42'S – 26°36'S segment was investigated by three vertical CTD casts, one tow-yo and one AUV dive (Figure 10). A turbidity plume rising ~280 m above the seafloor and strong ORP anomalies were discovered during tow-yo 48 traversing the axial high at 26°S of which the shallowest part is cross-cut by a series of ridge-parallel fault scarps (Figure 10a, c). The plume discovery motivated a dedicated AUV mission of densely spaced survey lines flown at 50 m altitude above the axial high (Figure 10a, b). The AUV and tow-yo turbidity data agree in the location of the densest particle cloud, above the center of the axial high (Figure 10b,c). The AUV detected an ORP anomaly of  $\Delta E = -19$  mV, coincident with a +0.05 °C temperature spike, at 26°0.99'S/13°51.17'W originating from the nearby Merian Vent Field, discovered during the MSM-25 cruise (green circle in Figure 10c; Devey and cruise-participants, 2013). Another ORP anomaly of  $\Delta E_h = -43$  mV, paralleled by a +0.03 °C temperature anomaly, was detected at 26°2.71'S/13°50.88'W (marked as Site II in Figure 10a-c) that is not accompanied by a particle plume.

Water samples collected during tow-yo 48 yield a  $\delta^3\text{He}$  maximum of 52.2 % in the center of the particle plume (bottle number 7; Figure 10c, d). Water samples from station 51 (Figure 10a, e) show increased  $\delta^3\text{He}$  values of up to 16.0 % at 3815 m depth (~20 m above the seafloor) which are likely unrelated to the plume above the axial high and suggest another undiscovered vent at the segment's southern end. Near-bottom current velocities above the axial high average around 12 cm s<sup>-1</sup>, with directions between NW and SW (Figure 10c). Predicted barotropic tidal currents average around 5 cm s<sup>-1</sup> and their directions evolve from NW to S over the course of the two-yo station (Figure 10c) suggesting that bottom currents above the axial high are not fully in phase with barotropic tides and a residual flow of westerly direction prevails.

The identified ORP anomalies suggest there is one further active hydrothermal fields on the axial high besides the Merian Vent Field (Site II; Figure 10a-c), following the definition of Baker et al. (2016) who consider venting sites separated more than 1 km as individual vent fields. The dense particle plume above axial high is likely created by the Merian Vent Field and dispersed by the W directed residual bottom currents. The absence of turbidity plumes above venting sites II and III could either be attributed to sparse sampling (flying at 50 m altitude, the AUV might have passed below such plumes) or a different, particle-poor type of venting.

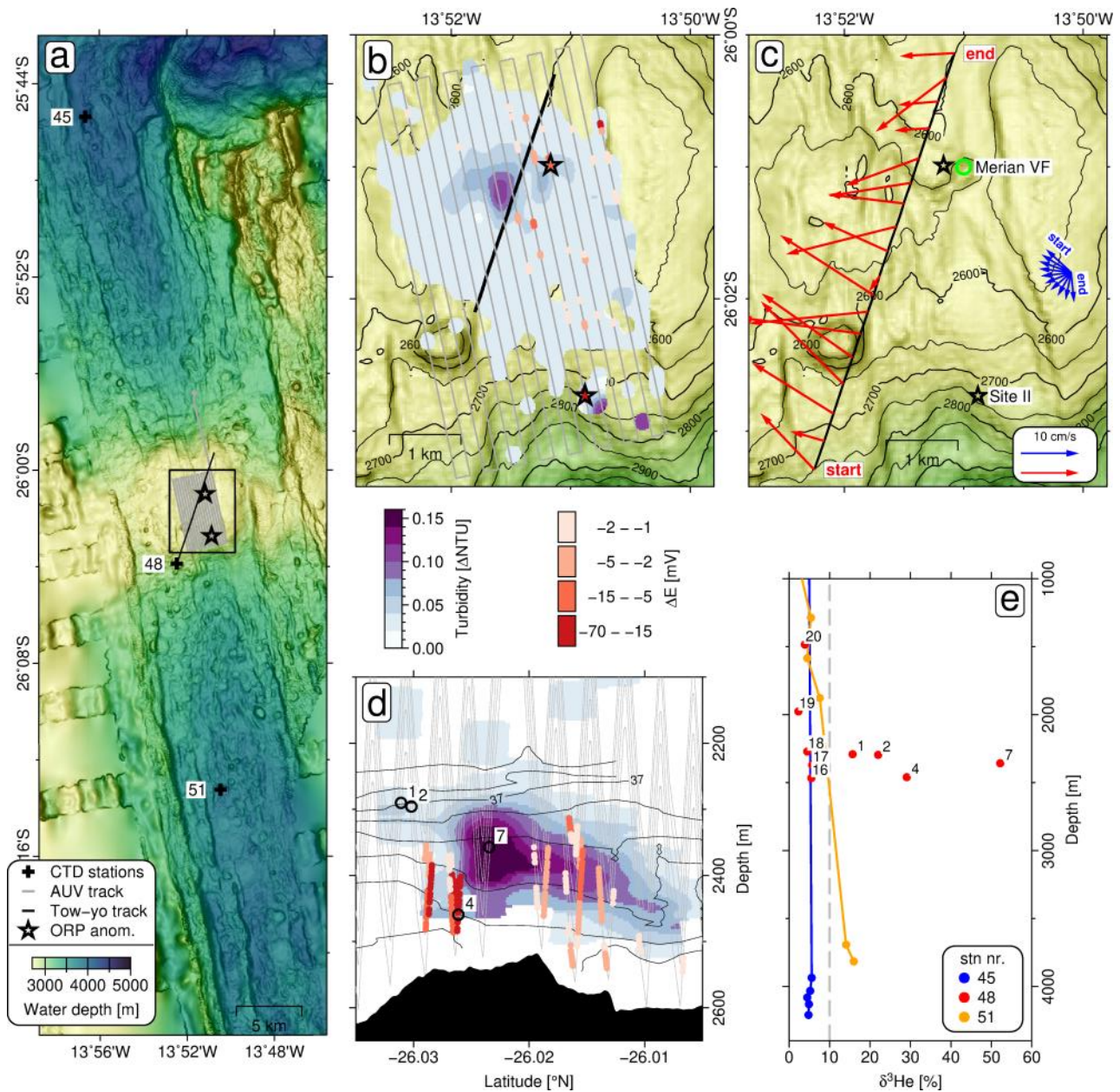


**Figure 10.** Results from the 25°42'S – 26°36'S segment. Map a gives an overview of the segment and the perimeter of maps b,c (black frame). Map b shows the AUV track (gray lines) and tow-yo track (black line). Blue shading, AUV turbidity data colored at the same scale as MAPR data in panel d and red dots  $\Delta E$  anomalies at the same color scale as MAPR data in panel d. Note, the AUV was flown at 50 m above seafloor and remained below the center of the turbidity plume. Map c, red vectors show average measured current velocities in the lowermost 200 m and blue arrows show predicted barotropic tidal current velocities. Green circle indicates the location of the Merian Vent Field (Devey and cruise-participants, 2013). Panel d, results from tow-yo 48 track plotted in c. Faint gray lines indicating MAPR tracks, blue shading representing turbidity and red dots showing  $\Delta E$  anomalies (color bars above). Numbered circles show water sampling locations and black contours are isopycnals. Panel e,  $\delta^3\text{He}$  profiles 45, 48 and 51 with labels corresponding to bottle numbers of station 48 in panel d.

### 5.3.9 MAR 2640'S – 27°50'S

In the 26°40'S – 27°50'S region was investigated by one AUV dive and four vertical CTD casts (Figure 11a). The AUV detected two ORP anomalies at 27° 8.86'S/13°28.52'W ( $\Delta E = -10$  mV) and at 27° 47.62'S/13°22.38'W ( $\Delta E = -30$  mV). The northern anomaly is accompanied by a 0.03  $\Delta$ NTU turbidity increase (Figure 11b). None of the water samples collected along the AUV track showed increased  $^3\text{He}$  concentrations (Figure 11d). Three water samples collected at station 42 (at 26°42.58'S/13°36.59'W) in water depths of 3250 - 3350 m yield  $\delta^3\text{He}$  values of 16.8 – 18.0 ‰. This  $^3\text{He}$  plume did not coincide with any turbidity or ORP anomalies but has a considerable rise height of ~500 m above the seafloor and suggests active hydrothermal venting in the vicinity of station 42.

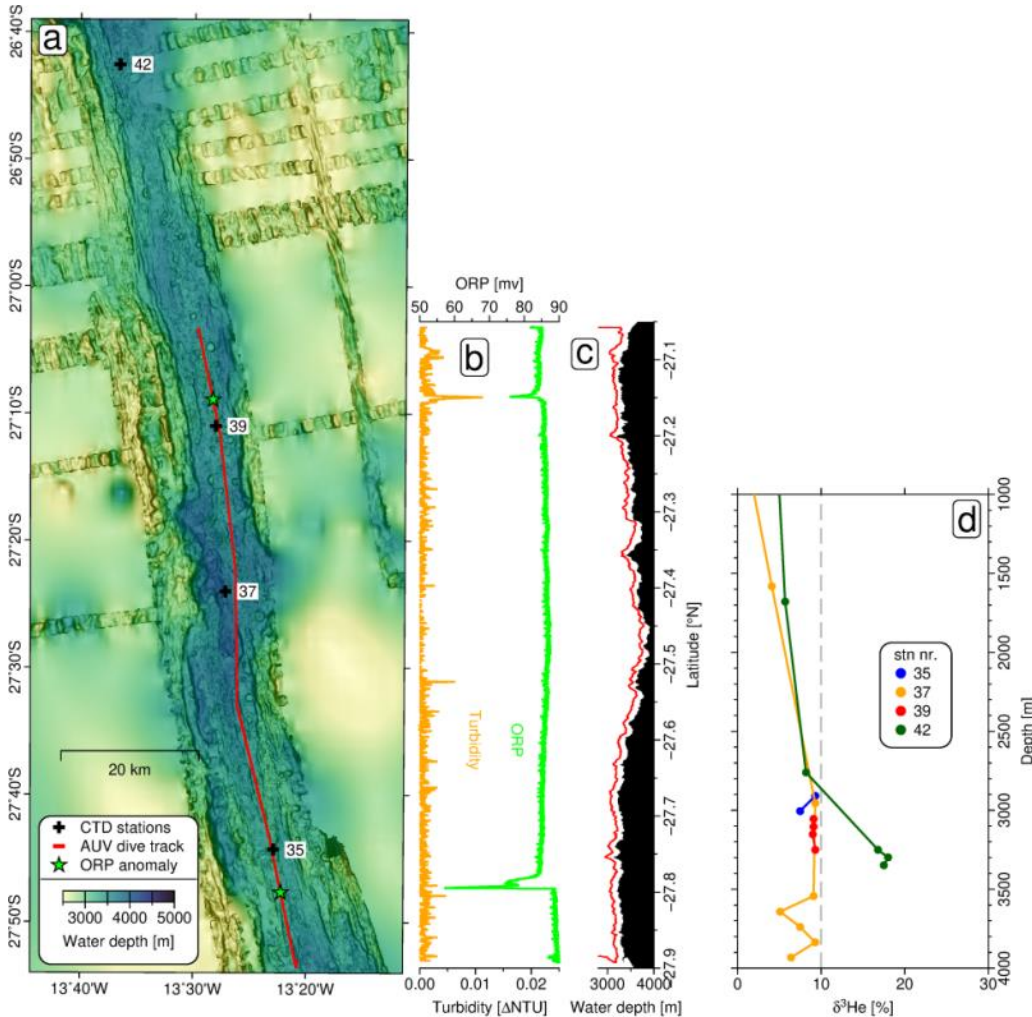


**Figure 11.** Results from the 26°40'S – 27°50'S region. Map a, bathymetry of the ridge segment with AUV track and CTD stations. Panel b, turbidity and ORP versus latitude along the AUV track. Panel c, vehicle- and seafloor depth versus latitude along the AUV track. Panel d, vertical profiles of  $\delta^3\text{He}$  for stations 35, 37, 39 and 42.

### 5.3.10 MAR 30°50'S

Vertical CTD 19 station was placed at the center of the ridge segment between 30°38'S and 31°13'S (Figure 12a). One water sample at 2809 m depth yielded a  $\delta^3\text{He}$  value of 12.8 % and the MAPR detected an ORP anomaly between 2805 – 2940 m depth, i.e. ~400 m above the seafloor (Figure 12b) but no coincident turbidity anomaly was detected. Although weak, we infer our findings give evidence for hydrothermal activity in the vicinity of station 19.

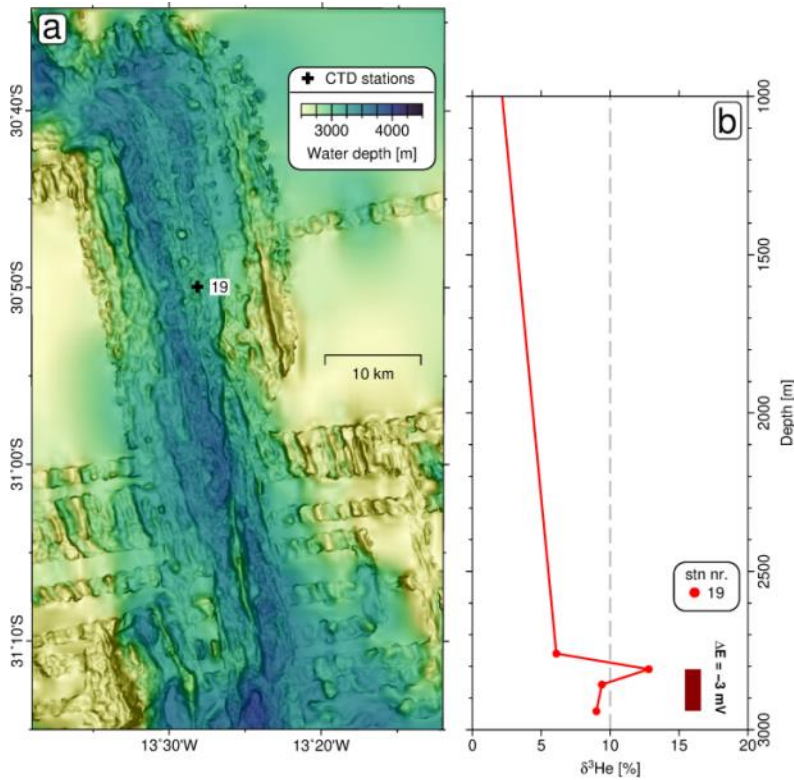


**Figure 12.** Results from the 30°50'S plume site. Map a, bathymetry of the ridge segment. Panel b shows  $\delta^3\text{He}$  results and the depth of an ORP anomaly at station 19.

### 5.3.11 MAR 31°40'S

The 30°15'S - 32°5'S segment was investigated by one long-range AUV dive and five vertical CTD casts (Figure 14a). A turbidity anomaly of 0.007  $\Delta\text{NTU}$  was found at 31°44.26'S/13°22.63'W in 2890 m water depth above an axial high at the segments center (Figure 13b, c). Since no ORP data is available from this AUV dive a coincident ORP anomaly cannot be confirmed. Water samples collected at station 14 (~3 km south of the turbidity anomaly) did not show an increase in  $^3\text{He}$  but a slightly increased  $\delta^3\text{He}$  value of 10.7 % was found at 3955 m depth at station 16 (Figure 13d) approximately 23 km north of the AUV turbidity anomaly. While it seems likely that there is hydrothermal activity at this ridge segment, we can only speculate about the vent location and whether the  $^3\text{He}$  signal at station 16 and the turbidity plume above the segment center have a common source or not. The increased  $\delta^3\text{He}$  value of 11.4 % at 3660 m depth (70 m above the seafloor) sampled at station 12 near the southern end of the segment seems too deep to originate from within the segment and may stem from an unknown source in the fracture zone (Figure 13a, d).

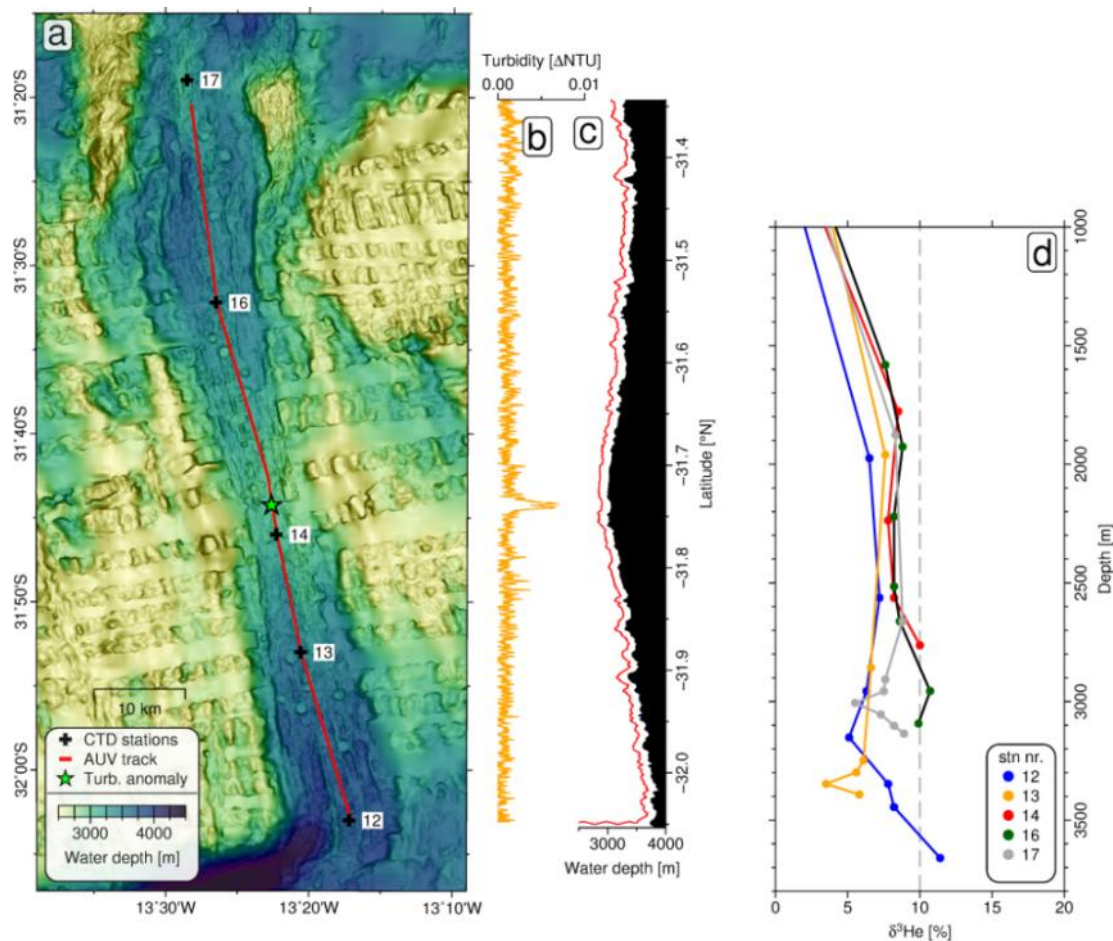


**Figure 13.** Map a gives an overview of the ridge segment, AUV track and CTD stations. Panel b, turbidity versus latitude along the AUV track. No ORP data is available from this dive. Panel c, vehicle- and seafloor depth versus latitude along the AUV track. Panel d, vertical profiles  $\delta^3\text{He}$  for stations 12 – 17.

### 5.3.12 MAR 33°S

The most southerly segment investigated (32°30'S-33°30'S) was surveyed by a long-range AUV mission, one tow-yo (6) and three vertical CTD casts (3, 5, 7; Figure 14a). The segment center is characterized by an axial volcanic high at which the seafloor is covered by numerous mounds of variable size (Figure 15a, b). During the AUV mission two distinct ORP anomalies were detected at 32°58.06'S/14°27.10'W ( $\Delta E = -72$  mV; Site I) and at 32°59.68'S/14°26.55'W ( $\Delta E_h = -32$  mV; Site II) that are marked by stars in Figure 14a, b. The ORP anomaly at Site I consists of three consecutive pulses within a strike distance of 650 m and the AUV CTD data revealed a +0.03°C spike in temperature coincident with the strongest ORP anomaly (Figure 14c). Sites I and II are associated with turbidity plumes and additional turbidity anomalies were found ~2 km and ~6 km north of Site I (Figure 14c). No turbidity or ORP signal was detected along tow-yo 6 (Figure 14a) but a  $\delta^3\text{He}$  value of 18.2 % was found at 2367 m water depth near the northern end of tow-yo 6 (Figure 14e). The three repeated ORP pluses and the temperature spike at Site I indicate a field of multiple active chimneys. The ORP, temperature and turbidity anomalies at Site II indicate another active vent field.

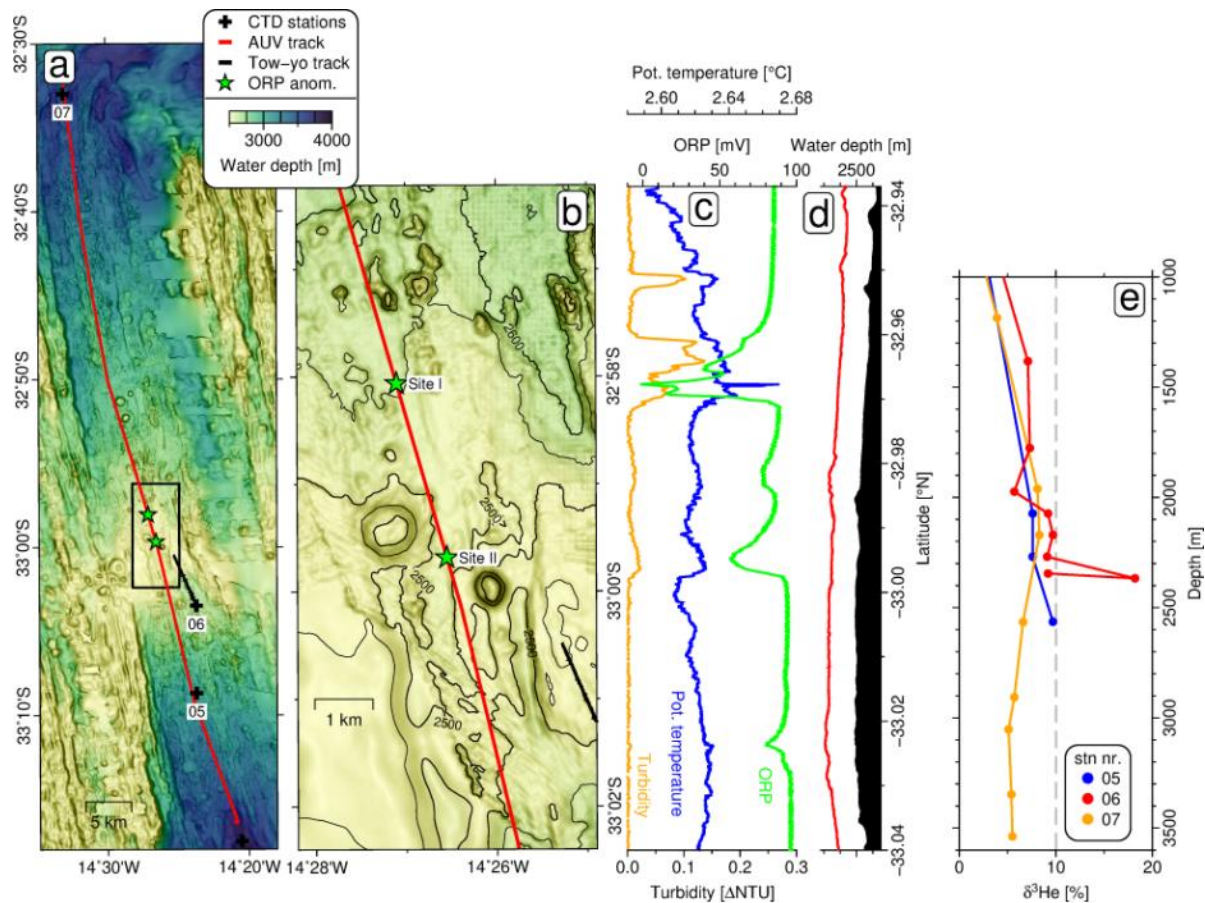


**Figure 14.** Results from the 33°S axial high. Map a, bathymetry of the ridge segment with black frame indicating perimeter of map b. Panel c, turbidity, potential temperature and ORP versus latitude along the AUV track displayed on map b. Panel d, vehicle- and seafloor depth versus latitude along the AUV track. Panel e, vertical profiles of  $\delta^3\text{He}$  for stations 5 – 7. Note, that no turbidity or ORP anomaly was detected at tow-yo station 6.

#### 5.4 Relation to Vent Field Frequency along the Global MORs

Our survey covered approximately 2100 km of the SMAR axis (excluding transforms) along which hydrothermal plumes were found at ten ridge segments, providing the location of 14 new and three previously known hydrothermal vent fields. A summary of all confirmed and inferred sites is given in Table 1, including the previously known Zouyu-1 and Rainbow Bay vent fields (Tao et al., 2011; Tao et al., 2017) that have not been visited during the MSM-25 cruise. We count a total number of 19 vent fields in the 13°-33°S region implying an average vent field incidence of 0.9 vent fields per 100 km ridge axis. With spreading rates of 32-34 mm yr<sup>-1</sup> in this region the inferred frequency matches well with the latest global compilations of vent field incidence (Beaulieu et al., 2015; Hannington et al., 2011; Figure 15).



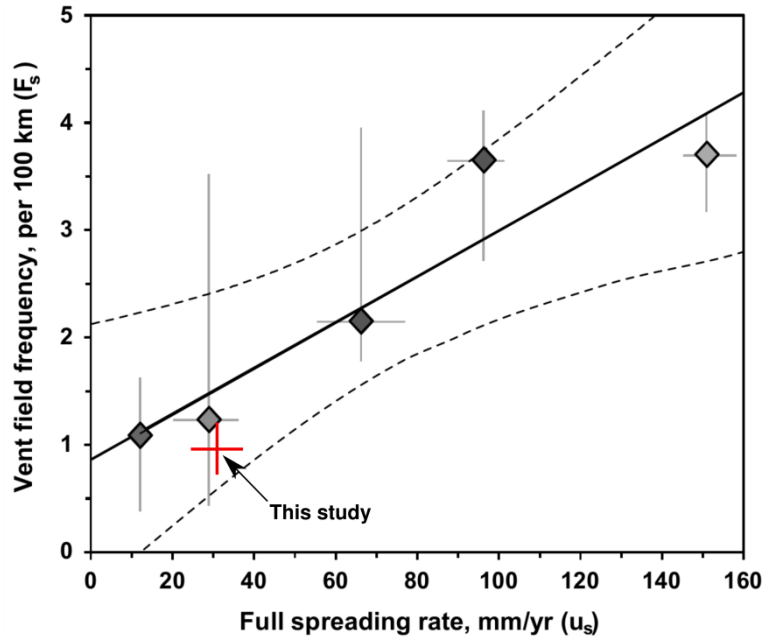


Figure 15. Relation of the vent field frequency in the 13°-33°S region of the SMAR to the vent field frequency along the global Mid-Ocean Ridges, compiled by Beaulieu et al., (2015). Diamonds represent hydrothermal survey results from non-hotspot influenced ridges binned into five spreading rate categories. Horizontal and vertical bars show give the range of data points for each category. Figure is from Beaulieu et al., (2015).

The actual number of vent fields in the 13°-33° region may even be higher, assuming our survey has missed odd sites. Sampling even in close proximity to active vents does not always return a plume signal, as demonstrated in the case of station 113 at ~1.5 km distance to the Deyin-1 vent site where no plume signal was found by our vertical CTD cast (Figure 5). Thus, our number of inferred vent fields may be considered a minimum estimate. Since the AUV dives and CTD stations focused on the center of the axial valley, we would also have not detected any off-axis systems, with the exception of the 23°S segment, where the off-axis core complex was specifically targeted with the AUV.

**Table 1.** Summary of all confirmed and inferred hydrothermal venting sites in the 13°-33°S region.

| (Prelim.) site name      | Seg. surveyed during MSM-25 | Inferred vent field locations      | Max turbidity [ $\Delta$ NTU] | Max $\Delta$ E [mV] | Max. $\delta^3\text{He}$ [‰] | Approx. seafloor depth of vent [m] | Approx. rise height of plume [m] | Tectonic setting               | MSM-25 CTD stations | MSM-25 AUV dive |
|--------------------------|-----------------------------|------------------------------------|-------------------------------|---------------------|------------------------------|------------------------------------|----------------------------------|--------------------------------|---------------------|-----------------|
| Zouyu-1 <sup>a</sup>     | 16                          | 13°15.0'S/14°24.6'W <sup>a</sup>   | -                             | -                   | -                            | 2300                               | unknown                          | Axial high                     | -                   | -               |
| Zouyu-2                  | 16                          | 13°17.31'S/14°24.59'W <sup>c</sup> | 0.14 (MAPR)                   | -56 (MAPR)          | 146.9                        | 2300                               | 200                              | Axial high                     | 124                 | #135            |
| Tai Chi                  | 16                          | 13°35.41'S/14°31.21'W <sup>e</sup> | 0.19 (MAPR)                   | -83 (MAPR)          | 29.5                         | 3180                               | 380                              | At eastern valley wall         | 122                 | -               |
| Rainbow Bay <sup>b</sup> | 16                          | 14°3.6'S/14°20.4'W <sup>b</sup>    | -                             | -                   | -                            | 2900                               | unknown                          | At eastern valley wall         | -                   | -               |
| Deyin-1                  | 15                          | 15°9.97'S/13°21.34'W <sup>d</sup>  | 0.06 (MAPR)                   | -20 (MAPR)          | 25.9                         | 2850                               | 350                              | Center of axial valley         | 116                 | #134            |
| MAR 17°S                 | 14                          | 17°15.13'S/14°13.62'W <sup>e</sup> | 0.008 (MAPR)                  | -21 (MAPR)          | 19.9                         | 3280                               | 280                              | Axial high                     | 107                 | -               |
| MAR 19°S                 | 12                          | 19°19.81'S/11°56.53'W <sup>d</sup> | 0.08 (AUV)                    | -22 (AUV)           | 22.8                         | 2700                               | unknown                          | At valley bottom               | 102                 | #133            |
| MAR 23°S                 | 9                           | 23°44.7'S/13°23.6'W <sup>d</sup>   | 0.08 (MAPR)                   | -61 (MAPR)          | 42.4                         | 2880                               | 350                              | on top of oceanic core complex | 070                 | #129            |
| MAR 25°S                 | 8                           | 25°20.10'S/13°37.83'W <sup>d</sup> | 0.02 (MAPR)                   | -31 (MAPR)          | none?                        | 2570                               | 200                              | Axial high                     | 054                 | -               |
| Merian Vent Field        | 7                           | 26°00.99'S/13°51.17'W <sup>d</sup> | 0.15 (MAPR)                   | -19 (AUV)           | 52.2                         | 2550                               | 280                              | Axial high                     | 048                 | #128            |
|                          | 7                           | 26°02.71'S/13°50.88'W <sup>d</sup> | unknown                       | -43 (AUV)           | unknown                      | 2750                               | unknown                          | Axial high                     | 048                 | #128            |
| MAR 26.2°S               | 7                           | 26°13.24'S/13°50.47'W <sup>d</sup> | unknown                       | unknown             | 16.0                         | 3825                               | unkown                           | unkown                         | 051                 | -               |
| MAR 26.7°S               | 7                           | 26°42.58'S/13°36.59'W <sup>d</sup> | unknown                       | unknown             | 18.0                         | 2400                               | 500                              | unkown                         | 042                 | -               |
| MAR 27°S                 | 6                           | 27°8.86'S/13°28.52'W <sup>d</sup>  | 0.03 (AUV)                    | -10 (AUV)           | unknown                      | 3400                               | unknown                          | At valley bottom               | 039                 | #127            |
| MAR 28°S                 | 6                           | 27°47.62'S/13°22.38'W <sup>d</sup> | none                          | -30 (AUV)           | unknown                      | 3100                               | unknown                          | Center of axial valley         | 035                 | #127            |
| MAR 30.8°S               | 2                           | 30°49.96'S/13°28.14'W <sup>e</sup> | none                          | -3 (MAPR)           | 12.8                         | 2950                               | 180                              | Center of axial valley         | 019                 | -               |
| MAR 31°S                 | 2                           | 31°44.26'S/13°22.63'W <sup>f</sup> | 0.007 (AUV)                   | unknown             | unknown                      | 3050                               | unknown                          | Axial high                     | Near 014            | #125            |
| MAR 33°S                 | 1                           | 32°58.06'S/14°27.10'W <sup>d</sup> | 0.13 (AUV)                    | -72 (AUV)           | unknown                      | 2600                               | unknown                          | Axial high                     |                     | #124            |
|                          | 1                           | 32°59.68'S/14°26.55'W <sup>d</sup> | 0.07 (AUV)                    | -32 (AUV)           | unknown                      | 2600                               | unknown                          | Axial high                     |                     | #124            |

<sup>a</sup>location from *Tao et al.* (2017). <sup>b</sup>location from *Tao et al.* (2011). <sup>c</sup>location of buoyant plume. <sup>d</sup>location of strong ORP anomaly. <sup>e</sup>location of CTD station detecting plume signal. <sup>f</sup>location of turbidity anomaly. Note, the Zouyu-1 and Rainbow Bay sites have not been visited during the MSM-25 but are listed here for completeness.

## 6 Conclusions

Knowing the seafloor location of active venting sites is a crucial prerequisite for the later planning of detailed studies on hydrothermal activity, biogeographical distribution of endemic vent fauna, and of seafloor massive sulfide deposits along MORs. We present the results of an over 2100 km-long systematic

plume survey in the 13°S-33°S region of the SMAR, a previously virtually unexplored ridge region. During expedition MSM-25 we identified previously unknown plumes above ten ridge segments and confirmed three previously known hydrothermal plumes using a combination of three independent hydrothermal tracers: ORP, turbidity and <sup>3</sup>He. The major advantage of combining these tracers is their independence and difference in behavior. ORP is best for the near field, turbidity is easiest to detect and <sup>3</sup>He is a fully conservative tracer. Upon careful evaluation of the plume data we were able to infer the approximate seafloor locations of 14 previously unknown and three known vent fields in the 13°S-33°S region. A majority of the explored sites are associated with morphologically pronounced axial volcanic highs, suggesting a close relationship between hydrothermalism and magmatism in this region. An exception is the inferred vent field at 23°S, located ~6 km off-axis, on top of the southernmost known oceanic core complex on the Mid-Atlantic Ridge.

A very unusual hydrothermal plume was observed above the extensive Zouyu Ridge axial volcanic high at 13°S. Redox anomalies are typically associated with low temperature venting and rise to lesser heights above the seafloor than particle plumes. A reverse vertical zonation was observed here, where an extended redox plume occurs ~50 m above the core of a particle plume. This may result from vertical age stratification in the plume (youngest at top, oldest at bottom) or the presence of two separate vents feeding the plume, one providing the particles, the other the reduced waters.

The average vent field frequency of 0.9 vents per 100 km ridge axis in the 13°-33°S region matches the vent field frequency predicted by global compilations of vent field incidence versus spreading rate. We conclude that the results from this reconnaissance study present a comprehensive overview of the locations of hydrothermal activity in the 13°S-33°S region of the SMAR.

The hydrography and absence of vent sites near the Rio de Janeiro Transform, cross-cutting the SMAR at 22°S, suggests that this region represents a physical barrier to the meridional dispersal of hydrothermal larvae and possibly constitutes the biogeographic boundary between the different vent fauna communities found in the North Atlantic and those at the Antarctic Ridges.

## Acknowledgments and Availability of Data

We acknowledge the captain and crew of RV Maria S. Merian expedition MSM-25. We are especially grateful to the GEOMAR AUV team and all other scientists of expedition MSM-25 for their contributions at sea. M. P. thanks O. Huhn for helpful advice on noble gas related matters. All data presented in this paper will be available via the PANGAEA earth data publisher (<https://pangaea.de>) once the manuscript has been accepted for publication. MAPRs were kindly provided by the NOAA vents program and the ORP sensor for the AUV was kindly provided by Ko-ichi Nakamura (AIST, Japan). Figures were created with the GMT software (Wessel et al., 2013). F. S. was funded through the DFG Cluster of Excellence ‘*Der Ozean im Erdsystem*’ at the University of Bremen, grant no. 49926684. M.W. was supported by DFG grant WA 2556/4. This is PMEL contribution 4920.

## References

- Baker, E. T. (2017), Exploring the ocean for hydrothermal venting: New techniques, new discoveries, new insights, *Ore Geology Reviews*, 86, 55-69, doi: 10.1016/j.oregeorev.2017.02.006.
- Baker, E. T., and C. R. German (2004), On the Global Distribution of Hydrothermal Vent Fields, edited by C. R. German, J. Lin and L. M. Parson, pp. 245-266, American Geophysical Union.
- Baker, E. T., Y. J. Chen, J. Phipps Morgan, and J. P. Morgan (1996), The relationship between near-axis hydrothermal cooling and the spreading rate of mid-ocean ridges, *Earth Planet. Sci. Lett.*, 142, 137-145, doi: 10.1016/0012-821X(96)00097-0.
- Baker, E. T., M.-H. Cormier, C. H. Langmuir, and K. Zavala (2001), Hydrothermal plumes along segments of contrasting magmatic influence, 15°20'-18°30'N, East Pacific Rise, *Geochemistry, Geophysics, Geosystems*, 2(9), doi: 10.1029/2000GC000165.
- Baker, E. T., J. A. Resing, R. M. Haymon, V. Tunnicliffe, J. W. Lavelle, F. Martinez, V. Ferrini, S. L. Walker, and K. Nakamura (2016), How many vent fields? New estimates of vent field populations on ocean ridges from precise mapping of hydrothermal discharge locations, *Earth and Planetary Science Letters*, 449, 186-196, doi: 10.1016/j.epsl.2016.05.031.
- Baker, E. T., S. L. Walker, J. A. Resing, W. W. Chadwick, S. G. Merle, M. O. Anderson, D. A. Butterfield, N. J. Buck, and S. Michael (2017), The Effect of Arc Proximity on Hydrothermal Activity Along Spreading Centers, *Geochemistry, Geophysics, Geosystems*, 18(11), 4211-4228, doi: 10.1002/2017GC007234.
- Beaulieu, S. E. (2015), InterRidge Global Database of Active Submarine Hydrothermal Vent Fields: prepared for InterRidge, Version 3.4, World Wide Web electronic publication, accessed 2018-06-22.
- Beaulieu, S. E., E. T. Baker, and C. R. German (2015), Where are the undiscovered hydrothermal vents on oceanic spreading ridges?, *Deep Sea Research Part II: Topical Studies in Oceanography*, 121, 202-212, doi: 10.1016/j.dsr2.2015.05.001.
- Beaulieu, S. E., E. T. Baker, C. R. German, and A. Maffei (2013), An authoritative global database for active submarine hydrothermal vent fields, *Geochemistry, Geophysics, Geosystems*, 14(11), 4892-4905, doi: 10.1002/2013GC004998.
- Broecker, W. S., T. Takahashi, and Y. H. Li (1976), Hydrography of the central Atlantic—I. The two-degree discontinuity, *Deep Sea Research and Oceanographic Abstracts*, 23(April), 1083-1104, doi: 10.1016/0011-7471(76)90886-X.
- Charlou, J. L., Y. Fouquet, H. Bougault, J. P. Donval, J. Etoubleau, P. Jean-Baptiste, A. Dapigny, P. Appriou, and P. A. Rona (1998), Intense CH<sub>4</sub> plumes generated by serpentinization of ultramafic rocks at the intersection of the 15°20'N fracture zone and the Mid-Atlantic Ridge, *Geochimica et Cosmochimica Acta*, 62, 2323-2333, doi: 10.1016/S0016-7037(98)00138-0.
- Copley, J. T., et al. (2016), Ecology and biogeography of megafauna and macrofauna at the first known deep-sea hydrothermal vents on the ultraslow-spreading Southwest Indian Ridge, *Scientific Reports*, 6, 39158, doi: 10.1038/srep39158.
- Corliss, J. B., et al. (1979), Submarine Thermal Springs on the Galapagos Rift, *Science*, 203(4385), 1073-1083, doi: 10.1126/science.203.4385.1073.

DeMets, C., R. G. Gordon, and D. F. Argus (2010), Geologically current plate motions, *Geophys. J. Int.*, 181, 1-80, doi: 10.1111/j.1365-246X.2009.04491.x.

Devey, C. W., and cruise-participants (2013), SoMARTerm: The Mid-Atlantic Ridge 13-33°S, *Maria S. Merian Berichte*, doi: 10.2312/cr\_msm25.

Devey, C. W., C. R. German, K. M. Haase, K. S. Lackschewitz, B. Melchert, and D. P. Connelly (2010), The relationships between volcanism, tectonism and hydrothermal activity on the Mid-Atlantic Ridge south of the equator, in *Diversity of hydrothermal systems on slow spreading ocean ridges*, edited, pp. 133-152.

Edmond, J. M., C. Measures, R. E. McDuff, L. H. Chan, R. Collier, B. Grant, L. I. Gordon, and J. B. Corliss (1979), Ridge crest hydrothermal activity and the balances of the major and minor elements in the ocean: The Galapagos data, *Earth and Planetary Science Letters*, 46(1), 1-18, doi: 10.1016/0012-821X(79)90061-X.

Edmonds, H. N. (2010), Chemical Signatures From Hydrothermal Venting on Slow Spreading Ridges, in *Diversity of Hydrothermal Systems on Slow Spreading Ocean Ridges*, edited, pp. 27-42.

Egbert, G. D., and S. Y. Erofeeva (2002), Efficient Inverse Modeling of Barotropic Ocean Tides, *Journal of Atmosphere and Ocean Technology*, 19, 183-204, doi: 10.1175/1520-0426(2002)019.

Elderfield, H., and A. Schultz (1996), Mid-Ocean Ridge Hydrothermal Fluxes and the Chemical Composition of the Ocean, *Annual Review of Earth and Planetary Sciences*, 24(1), 191-224, doi: 10.1146/annurev.earth.24.1.191.

Feely, R. A., G. J. Massoth, J. H. Trefry, T. Baker, J. Paulson, and T. Lebon (1994), Composition and sedimentation of hydrothermal plume particles from North Cleft segment, Juan de Fuca Ridge, *Journal of Geophysical Research: Oceans*, 99(B3), 4985-5006, doi: 10.1029/93JB02509.

Fisher, C., K. Takai, and N. Le Bris (2007), Hydrothermal Vent Ecosystems, *Oceanography*, 20(1), 14-23, doi: 10.5670/oceanog.2007.75.

Fouquet, Y., et al. (2010), Geodiversity of hydrothermal processes along the mid-atlantic ridge and ultramafic-hosted mineralization: A new type of oceanic Cu-Zn-Co-Au volcanogenic massive sulfide deposit, in *Geophysical Monograph Series*, edited, pp. 321-367.

German, C. R., and L. M. Parson (1998), Distributions of hydrothermal activity along the Mid-Atlantic Ridge: interplay of magmatic and tectonic controls, *Earth and Planetary Science Letters*, 160, 327-341.

German, C. R., S. Petersen, and M. D. Hannington (2016), Hydrothermal exploration of mid-ocean ridges: Where might the largest sulfide deposits be forming?, *Chemical Geology*, 420, 114-126, doi: 10.1016/j.chemgeo.2015.11.006.

Haase, K. M., et al. (2007), Young volcanism and related hydrothermal activity at 5°S on the slow-spreading southern Mid-Atlantic Ridge, *Geochemistry, Geophysics, Geosystems*, 8, doi: 10.1029/2006gc001509.

Hannington, M. D., J. Jamieson, T. Monecke, S. Petersen, and S. E. Beaulieu (2011), The abundance of seafloor massive sulfide deposits, *Geology*, 39(12), 1155-1158, doi: 10.1130/G32468.1.

Hasterok, D. (2013), A heat flow based cooling model for tectonic plates, *Earth and Planetary Science Letters*, 361, 34-43, doi: 10.1016/j.epsl.2012.10.036.

Jean-Baptiste, P., E. Fourré, J. L. Charlou, C. R. German, and J. Radford-Knoery (2004), Helium isotopes at the Rainbow hydrothermal site (Mid-Atlantic Ridge, 36°14'N), *Earth and Planetary Science Letters*, 221(1-4), 325-335, doi: 10.1016/S0012-821X(04)00094-9.

Jean-Baptiste, P., E. Fourré, A. Dapigny, J.-L. Charlou, and J. P. Donval (2008), Deepwater mantle 3 He plumes over the northern Mid-Atlantic Ridge (36°N-40°N) and the Azores Platform, *Geochemistry, Geophysics, Geosystems*, 9(3), 1-13, doi: 10.1029/2007GC001765.

Jean-baptiste, P., J. Charlou, M. Stievenard, J. P. Donval, H. Bougault, and C. Mevel (1991), Helium and methane measurements in hydrothermal fluids from the mid-Atlantic ridge: the Snake Pit site at 23° N, *Earth and Planetary Science Letters*, 106, 17-28, doi: 10.1016/0012-821X(91)90060-U.

Keir, R. S., J. Sültenfuß, M. Rhein, G. Petrick, and J. Greinert (2006), Separation of 3He and CH4 signals on the Mid-Atlantic Ridge at 5°N and 51°N, *Geochimica et Cosmochimica Acta*, 70, 5766-5778, doi: 10.1016/j.gca.2006.06.005.

Kelley, D. S., and T. M. Shank (2010), Hydrothermal systems: A decade of discovery in slow spreading environments, in *Diversity of Hydrothermal Systems on Slow Spreading Ocean Ridges*, edited, pp. 369-407.

Kelley, D. S., et al. (2001), An off-axis hydrothermal vent field near the Mid-Atlantic Ridge at 30° N, *Nature*, 412, 145-149., doi: Doi 10.1038/35084000.

Li, B., X. Shi, J. Wang, Q. Yan, and C. Liu (2018), Tectonic environments and local geologic controls of potential hydrothermal fields along the Southern Mid-Atlantic Ridge (12–14°S), *Journal of Marine Systems*, 181, 1-13, doi: 10.1016/j.jmarsys.2018.02.003.

Lupton, J. E. (1998), Hydrothermal helium plumes in the Pacific Ocean, *Journal of Geophysical Research: Oceans*, 103, 15853-15868, doi: 10.1029/98jc00146.

Lupton, J. E., and W. J. Jenkins (2017), Evolution of the south Pacific helium plume over the past three decades, *Geochemistry, Geophysics, Geosystems*, 18(5), 1810-1823, doi: 10.1002/2017GC006848.

Lupton, J. E., R. F. Weiss, and H. Craig (1977), Mantle helium in hydrothermal plumes in the Galapagos Rift, *Nature*, 267, 603, doi: 10.1038/267603a0.

McGillicuddy, D. J., J. W. Lavelle, A. M. Thurnherr, V. K. Kosnyrev, and L. S. Mullineaux (2010), Larval dispersion along an axially symmetric mid-ocean ridge, *Deep-Sea Research Part I: Oceanographic Research Papers*, 57(7), 880-892, doi: 10.1016/j.dsr.2010.04.003.

Melchert, B., et al. (2008), First evidence for high-temperature off-axis venting of deep crustal/mantle heat: The Nibelungen hydrothermal field, southern Mid-Atlantic Ridge, *Earth and Planetary Science Letters*, 275, 61-69, doi: 10.1016/j.epsl.2008.08.010.

Mercier, H., G. L. Weatherly, and M. Arhan (2000), Bottom water throughflows at the Rio de Janeiro and Rio Grande Fracture Zones, *Geophysical Research Letters*, 27(10), 1503-1506, doi: 10.1029/2000GL011402.

Moalic, Y., D. Desbruyères, C. M. Duarte, A. F. Rozenfeld, C. Bachraty, and S. Arnaud-Haond (2012), Biogeography revisited with network theory: Retracing the history of hydrothermal vent communities, *Systematic Biology*, 61(1), 127-137, doi: 10.1093/sysbio/syr088.

Mullineaux, L. S., K. G. Speer, A. M. Thurnherr, M. E. Maltrud, and A. Vangriesheim (2002), Mullineaux et al., Implications of cross-axis flow for larval dispersal along mid ocean ridges, 2002.pdf, *Cahiers de Biologie Marine*, 43(3-4), 281-284, doi: <https://archimer.ifremer.fr/doc/00000/898/>.

Roether, W., R. Well, and A. Putzka (2001), Correction to "Component separation of oceanic helium", *Journal of Geophysical Research: Oceans*, 106(C3), 4679-4679, doi: 10.1029/1999JC000080.

Roether, W., R. Well, A. Putzka, and C. Rüth (1998), Component separation of oceanic helium, *Journal of Geophysical Research: Oceans*, 103, 27931-27946, doi: 10.1029/98jc02234.

Roether, W., M. Vogt, S. Vogel, and J. Sültenfuß (2013), Combined sample collection and gas extraction for the measurement of helium isotopes and neon in natural waters, *Deep Sea Research Part I: Oceanographic Research Papers*, 76, 27-34, doi: 10.1016/j.dsr.2013.02.006.

Rona, P. A., G. Klinkhammer, T. A. Nelsen, J. H. Trefry, and H. Elderfield (1986), Black smokers, massive sulphides and vent biota at the Mid-Atlantic ridge, *Nature*, 321, 33-37, doi: 10.1038/321033a0.

Rüth, C., R. Well, and W. Roether (2000), Primordial <sup>3</sup>He in South Atlantic deep waters from sources on the Mid-Atlantic Ridge, *Deep Sea Research Part I: Oceanographic Research Papers*, 47, 1059-1075, doi: 10.1016/S0967-0637(99)00077-1.

Ryan, W. B. F., et al. (2009), Global multi-resolution topography synthesis, *Geochemistry, Geophysics, Geosystems*, 10(3), doi: 10.1029/2008GC002332.

Saito, M. A., A. E. Noble, A. Tagliabue, T. J. Goepfert, C. H. Lamborg, and W. J. Jenkins (2013), Slow-spreading submarine ridges in the South Atlantic as a significant oceanic iron source, *Nature Geoscience*, 6(9), 775-779, doi: 10.1038/ngeo1893.

Schmale, O., M. Walter, J. Schneider Von Deimling, J. Sültenfuß, S. L. Walker, G. Rehder, and R. Keir (2012), Fluid and gas fluxes from the Logatchev hydrothermal vent area, *Geochemistry, Geophysics, Geosystems*, 13(7), doi: 10.1029/2012GC004158.

Shank, T. M., D. J. Fornari, K. L. Von Damm, M. D. Lilley, R. M. Haymon, and R. A. Lutz (1998), Temporal and spatial patterns of biological community development at nascent deep-sea hydrothermal

vents (9° 50'N, East Pacific Rise), *Deep-Sea Research II*, 45, 465-515, doi: 10.1016/S0967-0645(97)00089-1.

Sültenfuß, J., W. Roether, M. Rhein, J. Sultenfuss, W. Roether, and M. Rhein (2009), The Bremen mass spectrometric facility for the measurement of helium isotopes, neon, and tritium in water, *Isotopes Environ Health Stud*, 45, 83-95, doi: 10.1080/10256010902871929.

Tao, C., et al. (2011), Two hydrothermal fields found on the Southern Mid-Atlantic Ridge, *Science China Earth Sciences*, 54, 1302-1303, doi: 10.1007/s11430-011-4260-8.

Tao, C., et al. (2017), Hydrothermal plume mapping as a prospecting tool for seafloor sulfide deposits: a case study at the Zouyu-1 and Zouyu-2 hydrothermal fields in the southern Mid-Atlantic Ridge, *Marine Geophysical Research*, 38, 3-16, doi: 10.1007/s11001-016-9275-2.

Tivey, M. (2007), Generation of Seafloor Hydrothermal Vent Fluids and Associated Mineral Deposits, *Oceanography*, 20(1), 50-65, doi: 10.5670/oceanog.2007.80.

Van Dover, C. L., C. R. German, K. G. Speer, L. M. Parson, and R. C. Vrijenhoek (2002), Evolution and Biogeography of Deep-Sea Vent and Seep Invertebrates, *Science*, 295(2002), 1253-1257, doi: 10.1126/science.1067361.

Visbeck, M. (2002), Deep Velocity Profiling Using Lowered Acoustic Doppler Current Profilers: Bottom Track and Inverse Solutions, *Journal of Atmosphere and Ocean Technology*, 19(section 2), 794-807, doi: 10.1175/1520-0426(2002)019.

Walker, S. L., E. T. Baker, J. Resing, K. Nakamura, and P. McLain (2007), A new tool for detecting hydrothermal plumes: An ORP Sensor for the PMEL MAPR, paper presented at AGU Fall Meeting Abstracts.

Walter, M., C. Mertens, U. Stöber, C. R. German, D. R. Yoerger, J. Sültenfuß, M. Rhein, B. Melchert, and E. T. Baker (2010), Rapid dispersal of a hydrothermal plume by turbulent mixing, *Deep Sea Research Part I: Oceanographic Research Papers*, 57, 931-945, doi: 10.1016/j.dsr.2010.04.010.

Wang, H., X. Li, F. Chu, Z. Li, J. Wang, X. Yu, and D. Bi (2017), Mineralogy, geochemistry, and Sr-Pb isotopic geochemistry of hydrothermal massive sulfides from the 15.2° S hydrothermal field, *Journal of Marine Systems*, 180, 220-227, doi: 10.1016/j.jmarsys.2017.02.010.

Wang, S., H. Li, S. Zhai, Z. Yu, Z. Shao, and Z. Cai (2017), Mineralogical characteristics of polymetallic sulfides from the Deyin-1 hydrothermal field near 15°S, southern Mid-Atlantic Ridge, *Acta Oceanologica Sinica*, 36(2), 22-34, doi: 10.1007/s13131-016-0961-3.

Well, R., and W. Roether (2003), Neon distribution in South Atlantic and South Pacific waters, *Deep-Sea Research Part I: Oceanographic Research Papers*, 50, 721-735, doi: 10.1016/S0967-0637(03)00058-X.

Well, R., W. Roether, and D. P. Stevens (2003), An additional deep-water mass in Drake Passage as revealed by <sup>3</sup>He data, *Deep-Sea Research Part I: Oceanographic Research Papers*, 50(9), 1079-1098, doi: 10.1016/S0967-0637(03)00050-5.

Wessel, P., W. H. F. Smith, R. Scharroo, J. Luis, and F. Wobbe (2013), *Generic Mapping Tools: Improved Version Released*, *Eos, Trans. Am. Geophys. Un.*, 94, 409-410, doi: 10.1002/2013EO450001.